Revision 2

Hydrothermal fluid signatures of the Yulong porphyry Cu-Mo deposit: Clues from the composition and U-Pb dating of W-bearing rutile

Qi Chen[1], Changming Wang[1,*], Leon Bagas[1,2], Bin Du[1,3], Kangxing Shi[1], Jiaxuan Zhu[1]

[1] *State Key Laboratory of Geological Processes and Mineral Resources, China University of Geosciences (Beijing), Beijing 100083, China*

[2] *Xi'an Center of Mineral Resources Survey, China Geological Survey, Xi'an 710054, China*

[3] *China Non-ferrous Metals Resource Geological Survey, Beijing 100012, China*

* Corresponding author: Changming Wang

Phone: (+86-10) 8232 2301 (O)

Email: wangcm@cugb.edu.cn

Abstract

Hydrothermal rutile (TiO_2) is a widely distributed accessory mineral in hydrothermal veins or alteration assemblages of porphyry deposits and provides important information for further understanding hydrothermal fluid signatures. This study investigates the geochemical composition and U–Pb dates of hydrothermal rutile from the Yulong porphyry Cu-Mo deposit in east

Tibet, China. The three types of TiO_2 polymorphs distinguished at the deposit by their Raman spectroscopy, textural and chemical characteristics are: (1) brookite and anatase pseudomorphs after titanite in a fine-grained matrix, indicating low-temperature hydrothermal fluids destabilizing primary Ti-bearing minerals during argillic alteration (type-I); (2) elongated and prismatic rutile present in hydrothermal veins or in clusters in accompanying alteration envelope characterized by weak zoning (type-II); and (3) rutile intergrown with sulfides in hydrothermal veins, characterized by well-developed patchy and sector zoning (type-III). In contrast to the type-I and type-II TiO_2 polymorphs, tungsten is enriched in back-scatter bright patches and sector zones in type-III rutile, which is due to the substitution of W^{6+} in the Ti^{4+} octahedral site. The mechanism of the enrichment of tungsten is effectively driven by the halogen-rich (F, Cl) aqueous fluids during hydrothermal mineralization. *In situ* U-Pb dating of the type-III rutile yields a lower intercept age of 41.8 ± 1.2 Ma, which brackets the timing of the Cu-Mo mineralization. The relationship between rutile textures and composition indicates that W-bearing rutile can serve as a recorder of hydrothermal processes in porphyry Cu deposits.

Keywords: W-bearing rutile, Hydrothermal fluid signatures, U-Pb geochronology, EMPA, Mineral chemistry, Porphyry Cu-Mo deposits

Introduction

Rutile is a widely distributed accessory mineral, found in metamorphic, sedimentary, and igneous rocks (Zack et al., 2004; Meinhold, 2010; Zack and Kooijman, 2017; Pe-piper et al., 2019) and formed in many magmatic-hydrothermal ore deposits, such as porphyry deposits (Scott, 2005; Rabbia et al., 2009; Schirra and Laurent, 2021; Wang et al., 2021). Previous studies have confirmed that rutile can form as a replacement product of Ti-bearing oxides and silicates (such as ilmenite, titanite or biotite), and contains variable concentrations of Fe, V, high field strength elements (HFSE), transition, and base metallic elements (Luvizotto and Zack, 2009; Meinhold, 2010; Plavsa et al., 2018; Agangi et al., 2019). The variable concentrations of trace elements are closely connected to the composition of the primary minerals, type and composition of magmatic and metamorphic fluids (Cl- or F-rich), pressure and temperature conditions, and oxygen fugacity (fO_2) (Zack et al., 2002, 2004; Plavsa et al., 2018; Majzlan et al., 2021). Therefore, rutile enriched in V, W, Mo, Sn and Sb can be used as a geochemical fingerprint of a hydrothermal fluid associated with mineralization (c.f. Czamanske et al., 1981; Clark and Williams-Jones, 2004; Scott, 2005; Scott et al., 2011; Agangi et al., 2019).

Studies of rutile associated with porphyry Cu deposits have already been attempted using: (a) the trace element signature of the rutile as an indicator of mineralization (Rabbia et al., 2009; Schirra and Laurent, 2021); and (b) direct

63 U-Pb dating of rutile associated with sulfides to constrain the timing of the
64 hydrothermal mineralization events (Schirra and Laurent, 2021). Studies of
65 variations in, and incorporation mechanism of, these pathfinder elements in
66 rutile in porphyry deposits are still very limited. For example, individual rutile
67 commonly contains well-developed patchy and sector zonation reflecting the
68 distributions of various elements (e.g. W, Fe; Mercer and Reed, 2013).
69 Nonetheless, the modification of these elements driven by hydrothermal fluids
70 is poorly understood. Published studies have reported that hydrothermal rutile
71 containing up to 3 wt% tungsten content in porphyry deposits closely coexists
72 with sulfides, such as the Butte deposit in the USA (Mercer and Reed, 2013).
73 However, there is still a lack of understanding of the genesis of W-bearing
74 rutile in hydrothermal veins, including its distribution, substitution mechanism
75 and source of W. Answers to the above-mentioned problems are potentially
76 helpful in understanding the critical contributions of hydrothermal fluids to
77 mineralization in porphyry deposits, and defining vectors to undiscovered
78 systems.

79 The world-class Yulong Cu-Mo porphyry deposit (Fig. 1) is hosted by an
80 extensional (post-collisional) strike-slip fault zone in eastern Tibet, and has
81 been the focus of extensive studies and exploration in recent years (Tang and
82 Luo, 1995; Hou et al., 2003, 2006; Li et al., 2012; Chang et al., 2017, 2018;
83 Huang et al., 2019). A variety of minerals existing in porphyries, hydrothermal

84 veins or alteration halos have been used to constrain the magmatic and
85 hydrothermal processes operating during the genesis of the deposit (Huang et
86 al., 2019). This includes: (i) the accurately determined age and duration of
87 molybdenite crystallization in the deposit (Chang et al., 2017); (ii) the evolution
88 of the mineralizing magmatic-hydrothermal fluids and metal precipitation
89 based on the study of fluid inclusions in quartz (Sun et al., 2021); and (iii)
90 constraints on the time scales of individual magmatic phases and fluid pulses
91 using Ti diffusion in quartz (Chen et al., 2021). Although rutile is abundant in
92 altered porphyries and hydrothermal veins that are closely related to
93 mineralization, its origins, mineralogical characteristics, and the nature of
94 mineralization processes are poorly understood.

95 In this study, petrographically well-characterized hydrothermal rutile and
96 other TiO_2 polymorphs were collected from highly mineralized porphyries and
97 veins from Yulong for detailed analysis. The techniques used include: (i)
98 scanning electron microscopy-backscattered electron (SEM-BSE) imaging
99 and Raman spectroscopy analysis for textural and mineralogical analysis; (ii)
100 electron microprobe analysis (EMPA) and mapping to quantify element
101 abundances; and (iii) *in situ* dating of hydrothermal rutile by laser ablation-
102 inductively coupled plasma-mass spectrometry (LA-ICP-MS) to directly
103 determine the U-Pb ages of hydrothermal activity and Cu-Mo mineralization.
104 The data collected are then used to define the processes involved in the

incorporation of trace elements, such as W, to gain a better insight into the evolution of hydrothermal systems that lead to a fertile porphyry deposit.

Geological background

The Yulong deposit is situated in a 15-30 km wide and 300 km long zone containing porphyry Cu deposits. The zone is in the Qiangtang Terrane within the Himalayan-Tibetan Orogen (Tang and Luo, 1995; Hou et al., 2003; Fig. 1a). The deposits are spatially and temporally associated with over 100 Eocene porphyry intrusions and K-rich mafic to felsic volcanic rocks. The intrusions are hosted by N- to NNW-trending regional strike-slip faults, which are related to the culmination of the Paleocene to Eocene Eurasian-Indian continental collisional event (Hou et al., 2003; Yang et al., 2014; Wang et al., 2014, 2016, 2018a; Deng et al., 2017, 2018). The intrusions have LA-ICP-MS zircon U-Pb ages that decrease from ca. 44 Ma in the northwest to ca. 37 Ma approximately 100 km to the SE (Liang et al., 2006; Fig. 1b).

The mineralized zone includes several medium, large, and giant Cu(-Mo-Au) deposits, which are interpreted as being associated with a post-subduction or post-collisional setting (Hou et al., 2015; Lu et al., 2015; Wang et al., 2018b). The Yulong deposit is the third largest porphyry-type Cu-Mo deposit in China, containing a resource of > 1 Gt with an average grade of 0.62% Cu, 0.04% Mo and 0.05 g/t Au (Yang and Cooke, 2019). The deposit is

126 hosted by the Yulong Granite, which is subdivided into a porphyritic
127 monzogranite, with lesser amounts of porphyritic quartz monzonite, and rare
128 dykes of porphyritic quartz gabbro recognized at depth (Fig. 1c; Tang and
129 Luo, 1995; Chang et al., 2017).

130 Intrusion of the Yulong Granite was structurally controlled by several ring-
131 shaped, steeply dipping faults at the southern end of the N- to NW-trending
132 Hengxingcuo Anticline (Fig. 1c). The granite intrudes Triassic carbonate and
133 clastic rocks, and was emplaced at a depth of 1 to 3 km (Hou et al., 2003).
134 The deposit is characterized by concentric alteration zones ranging from an
135 inner K-silicate zone through a sericite and argillic zone to an outer propylitic
136 zone. The highest Cu-Mo grades are present in the porphyritic monzogranite
137 and faults around the pipelike orebody (Fig. 1d–e).

138 The porphyritic monzogranite hosts the majority of the Cu and Mo
139 mineralization at the Yulong deposit (Fig. 2a-b; Chang et al., 2017; Chen et
140 al., 2021; Sun et al., 2021). The deposit includes multiple stockwork veins,
141 such as the early EB veins associated with biotite alteration (Fig. 2c), the A
142 veins which consist of K-silicates (Fig. 2c), and the B veins which are
143 associated with chlorite-sericite alteration selvages (Fig. 2d; Chen et al.,
144 2021). Anatase and brookite polymorphs of TiO_2 found in the altered and
145 mineralized porphyritic monzogranite form accessory minerals replacing
146 altered titanite (Fig. 3b, c). In addition, a larger proportion of rutile is

commonly present within or along the edge of medium- to high-temperature EB, A, and B quartz veins containing abundant sulfides. The occurrence of rutile in these veins shows that its genesis is closely related to the main stage of the Cu-Mo mineralization. Significantly, there is hardly any rutile in the late D veins formed at low temperatures.

Sampling and Analytical Methods

Samples

Representative samples of core were collected from two diamond-drillholes and from depth in the Yulong mine. Eight thin and polished sections of rutile-bearing porphyritic monzogranite and hydrothermal veins were selected by microscopic examination for BSE, Raman and EMPA analysis. Three rutile-bearing samples of hydrothermal veins were selected for U-Pb dating and trace element analysis by LA-ICP-MS. Detailed sample locations and descriptions are provided in Figure 1 and Table S1.

SEM-backscattered electron

All the rutile grains analyzed in this study were from the polished 70-μm-thick sections, which revealed the textural and genetic context of rutile associated with the Yulong Cu-Mo mineralization. The polished thin sections were coated with carbon for BSE imaging using a Tescan GAIA3 SEM-FIB equipped with an Oxford Instruments CL detector at the Beijing Research

Institute of Uranium Geology, (BRIUG), China. Images were acquired in BSE mode with an accelerating voltage of 15 keV and a primary beam current of 20 nA.

Raman spectroscopy analysis

Studies of Raman spectra yielded information on the mineral structures indistinguishable from microscopy and BSE imaging. The polymorphs of the Ti-oxide were confirmed using a LabRam HR800 Raman micro-spectrometer with a Zeiss microscope at the Institute of Geology and Geophysics, Chinese Academy of Sciences (IGGCAS), Beijing, China. The exciting radiation was provided by an argon ion laser with a wavelength of 532 nm and a source power of 44 mW. Phase identification used Raman wavenumbers at 143, 241, 443, and 612 cm^{-1} for rutile, 144, 197, 400, 516 and 640 cm^{-1} for anatase, and 153, 247, 322 and 636 cm^{-1} for brookite (Meinhold, 2010).

Electron microprobe analysis and element mapping

The major and minor element compositions of rutile and other minerals in polished sections were analyzed using a JEOL JXA-iHP200F EMPA at the Institute of Mineral Resources, Chinese Academy of Geological Sciences. For the analyses of biotite, magnetite, hematite and sericite, the accelerating voltage was 15 keV at a beam current of 20 nA, with beam spots of 1–10 μm. Counting times were 10–30s on peak and half of this time on the respective

188 backgrounds, depending on the element and mineral analyzed. Natural
189 minerals and synthetic oxides were used as standards for calibration.
190 In order to obtain a lower detection limit for rutile crystals, the beam
191 current and counting time were accordingly increased with analysis conditions
192 of 15 keV accelerating voltage, 100 nA beam current, and 1 μm beam spot
193 (Zack et al., 2004). The counting times for Si, Zr, Ti, Nb, Fe, Cr, Ta, W, and V
194 are 90, 300, 15, 300, 150, 150, 300, 150 and 150s, respectively, with
195 respective detection limits of 23, 22, 253, 28, 49, 52, 29, 58 and 41 ppm.
196 Natural andradite was used as a Si standard, natural rutile was used as a Ti
197 standard, Natural eskolaite was used as a Cr standard, synthetic magnetite
198 was used for Fe, synthetic zircon was used as a Zr standard, and pure metals
199 were used for W, Nb, and Ta standards. All mineral formulas were
200 recalculated using the MINPET 2.0 software. High-sensitivity, low-resolution
201 element mapping of imaging was carried out using similar analysis conditions
202 to the spot analyses, and consumed ~4 hours of instrument time for every
203 sample.

204 **U-Pb dating and trace element analysis**

205 Rutile U-Pb isotopic and trace-element measurements were carried out
206 simultaneously using the LA-ICP-MS at the Nanjing Hongchuang Exploration
207 Technology Service Co., Ltd. Radiometric data were obtained using a
208 Wavelength Resonetics Resolution SE 193 nm Deep ultraviolet laser (Applied

Spectra, the USA) coupled to an Agilent 7900 (the USA) quadrupole ICP-MS. Pre-ablation was conducted for each spot analysis using 5 laser shots (~0.3 μm in depth) to remove potential surface contamination. The analysis was performed using 30 μm diameter spot at 5 Hz with fluence of 3 J/cm^2. Analyses were conducted over 20s background collection and 35-40s ablation periods. The ablated material was carried by helium gas and subsequently mixed with argon prior to input into the plasma. Trace-element concentrations were determined using the rutile RMJG and NIST SRM 610 as a calibration standard and to correct for any instrumental drift, mass bias and elemental fractionation. Measured masses included ^{49}Ti, ^{27}Al, ^{28}Si, ^{51}V, ^{52}Cr, ^{56}Fe, ^{90}Zr, ^{93}Nb, ^{95}Mo, ^{118}Sn, ^{121}Sb, ^{178}Hf, ^{181}Ta, ^{182}W, ^{202}Hg, ^{204}Pb, ^{206}Pb, ^{207}Pb, ^{208}Pb, ^{232}Th, and ^{238}U with a total sweep time of ~0.23s. The internal standard was ^{49}Ti with a content assumed as being stoichiometric. Every group of ten spots on unknows was bracketed by two analyses of the rutile RMJG standard (1758.4 ± 9.7 Ma, 2σ; Zhang et al., 2020) and two analyses of NIST SRM 610 glass standard. Reduction of both trace-element and U–Pb data was performed using the Iolite v2.5 software (Paton et al., 2011). The age calculations and plotting of concordia diagrams were completed using the ISOPLOT software (version 3.6; Ludwig, 2008). Common lead uncorrected data were used to construct a Tera-Wasserburg plot to calculate the lower intercept and U–Pb age. The initial ^{207}Pb/^{206}Pb common lead ratio was used

for single spot age calculations (Williams, 1998). Errors are quoted at the 2σ (95% confidence) level and are propagated from all sources except mass spectrometer sensitivity and flux monitor. Full isotopic and trace-element data for the standards and samples are given in Table S3.

Results

Occurrence and texture

Rutile and other TiO_2 polymorphs from Yulong, hydrothermal minerals in the altered porphyry and quartz veins, have variable textures and trace element compositions (see Table 1). All the analyzed TiO_2 polymorphs are typically deep reddish-brown and subhedral to anhedral in shape, varying from below 20 μm to over 300 μm in diameter (Fig. 3). The three types of TiO_2 polymorphs identified based on their petrographic characteristics and mode of occurrence are: (i) the type-I TiO_2 minerals with the same micro-Raman spectra as brookite and anatase (Fig. 5a–b); and (ii) both the type-II and type-III composed of rutile crystals, but the Raman intensity is slightly different at different positions (Fig. 5c–d). For example, the intensity of ~442 cm^{-1} wavenumber of W-rich rutile in type-III is significantly higher than that of W-poor rutile, and W-rich rutile has a peak at ~681 cm^{-1} wavenumber.

The type-I brookite and anatase typically form pseudomorphs of titanite crystals in a fine-grained matrix of altered porphyry (Fig. 3a–c). The titanite is

not completely replaced by polymorphs that contain monazite and sporadic amounts of sulfides (e.g. chalcopyrite, Fig. 3b). The brookite and anatase are subhedral and fine grains display homogeneous BSE intensity (Fig. 3b, c).

The type-II rutile commonly forms elongated and prismatic grains, and appears alone in hydrothermal veins or in clusters accompanying alteration envelopes (Fig. 3d, e). The rutile coexists with relict titanite and displays irregular and faint zoning on BSE images (Fig. 3d, f).

The type-III rutile is anhedral forming irregular grains in hydrothermal veins. Blocky rutile grains are hosted by biotite, sericite, and hematite, and are typically associated with the breakdown of Ti-rich minerals such as biotite and ilmenite (Fig. 3g–i). Many rutile grains are also intergrown with or included in sulfides such as pyrite, chalcopyrite and molybdenite in B veins (Fig. 3j–o). The type-III rutile displays well-developed zoning patterns including patchy, faint, oscillatory and sector zoning (Fig. 3h, k, l, n), as found in other porphyry deposits, for example at El Teniente, Butte, and El Salvador (Rabbia et al., 2009; Mercer and Reed, 2013; Schirra and Laurent, 2021). Small rutile grains are seen intergrown with hydrothermal minerals such as zircon, apatite, and anhydrite in hydrothermal veins (Fig. 4a–c), but are rarely associated with magnetite (Fig. 4d).

Major and minor element composition

In situ chemical analyses of rutile carried out using EMPA are shown in Figure 6 and summarized in Table S2. Concentrations of most trace elements are heterogeneous within each sample and each type. The type-I brookite and anatase in the porphyritic monzogranite contain high Si (up to 0.89 wt%) and Zr (up to 0.28 wt%) contents, but low Cr (<0.05 wt%), Ta (<0.05 wt%), and W (<0.01 wt%) contents. The type-II rutile has a similar range of Fe and Ta contents as the type-I brookite and anatase, but slightly higher V, Cr, and W contents. The type-III rutile in veins contain significantly variable Fe (0.39–3.51 wt%), V (0.84–1.80 wt%), Nb (0.07–4.89 wt%) and W (0.12–7.11 wt%) contents, but low Zr (<0.07 wt%), Si (<0.11 wt%), Cr (<0.52 wt%) and Ta (<0.14 wt%) contents. Compared with the type-II rutile, the type-III rutile has significantly higher V and W, and more variable Fe contents (Table S2). For the purpose of comparison, the type-III rutile is subdivided into W-rich and W-poor rutile.

The three types of rutile at Yulong show a negative correlation between W and Ti (Fig. 6a), whereas the V contents only display an obvious negative correlation with Ti in the type-III W-rich rutile (Fig. 6b). In addition, the type-II rutile has a more variable Nb content, and the concentrations of V and Nb cannot be correlated (Fig. 6c). The W and V contents of the other type-II and type-III rutile appear to be positively correlated (Fig. 6d). The V contents of all

the types of rutile increase with increasing W contents. The W-rich type-III rutile has higher V and Fe contents, but lower Nb contents than type-II and W-poor type-III rutile grains (Fig. 6e). In addition, the type-I data cluster in the 2s field for brookite, and most of the data from the type-II and -III grains cluster in the 2s field for rutile (Fig. 6f) from Triebold et al. (2011).

The EMPA mapping indicates that the elements are unequally distributed in the apparent homogeneous, faint, or patchily zoned type-II and III rutile grains (Fig. 7). High concentrations of trace elements are displayed on the EMPA images as warm colors (red, yellow, green) and the low concentrations appear as cool colors and tones (blue, purple, black). For example, the bright zones in the BSE images of the rutile grains interlocking with biotite contain more W than darker zones, and patches with variable bright zones locally show elevated V and Nb values (Fig. 7b). Similar element mapping results are also found in rutile intergrown with other minerals (Figs. A1–A2).

Biotite, magnetite, and other alteration minerals associated with rutile were scanned with the EMPA (Table S2). The results show that the TiO_2 content of magnetite in ore-bearing porphyry and quartz (EB) veins is generally low (<0.24 wt%). In contrast, the hydrothermal biotite is enriched in Ti (1.16-2.68 wt% TiO_2). The Ti content of sericite and hematite in hydrothermal alteration zones is also generally low (<0.4 wt%).

311 **LA-ICP-MS U-Pb Dating**

312 Seventeen U-Pb isotopic analyses were completed on vein-hosted type-III
313 rutile (samples 18-23B6, 1103B3, and 17-08B10). Results of U-Pb dating and
314 concordia diagrams are presented in Figure 8 and Table S3. The rutile
315 analyzed in this study has variable U contents (10.5–173 ppm) and variable
316 percentages of radiogenic ^{206}Pb, but a generally high proportion of common
317 lead as reflected by the spread of the discordant data points. Three analyses
318 were disregarded owing to high concentrations of common Pb, low U and the
319 presence of Si-rich inclusions. On the Tera-Wasserburg plot, linear regression
320 of the uncorrected data of 14 analyses yields a lower intercept age of 41.8 ±
321 1.2 Ma (2σ, MSWD = 1.2) with an initial $^{207}Pb/^{206}Pb$ ratio of 0.8059 ± 0.015
322 (Fig. 8a–c), which was used to calculate individual spot ages that yielded the
323 weighted average $^{206}Pb/^{238}U$ age of 41.3 ± 1.1 Ma (2σ, MSWD = 0.6, Fig. 8c).

324 **Discussion**

325 **Rutile U–Pb geochronology related to Cu-Mo mineralization**

326 Prior studies have constrained the timing of magmatism and Cu-Mo
327 mineralization at the Yulong deposit (Tang and Luo, 1995; Hou et al., 2003;
328 Chen et al., 2021 and references therein). The ages of the ore-bearing
329 porphyry have been constrained within a ca. 3.6 Ma time span bracketed by
330 U-Pb zircon LA-ICP-MS/SHRIMP dating from the earliest porphyritic
331 monzogranite dated at 43.8 ± 0.7 Ma (Wang et al., 2009) to the porphyritic

This is the peer-reviewed, final accepted version for American Mineralogist, published by the Mineralogical Society of America.
The published version is subject to change. Cite as Authors (Year) Title. American Mineralogist, in press.
DOI: https://doi.org/10.2138/am-2022-8453. http://www.minsocam.org/

quartz gabbro dated at 40.2 ± 0.3 Ma (Chang et al., 2017). The barren porphyritic monzonite at Ganlongla over 1 km to the north is coeval with the ore-bearing porphyritic monzogranite (Figs. 1a and 8d). Previous ID-ICP-MS and recent high-precision ID-NTIMS Re-Os molybdenite dating show that the deposit was mineralized over a period of ~5.1 million years (Hou et al., 2006; Chang et al., 2017). The bulk of the Cu-Mo mineralization, therefore, developed in a period of ca. 1.4 million years from the early-stage $A2_E$ veins dated at 42.3 ± 0.2 Ma to transitional stage B_T veins dated at 40.9 ± 0.2 Ma (Fig. 8d; Chang et al., 2017). Furthermore, the high-precision Re-Os molybdenite age of ca. 41 Ma does not bracket the complete age of the mineralizing event (Fig. 8d; Chiaradia et al., 2014; Schirra and Laurent, 2021).

Most rutile crystals at the Yulong deposit formed broadly synchronously with hydrothermal quartz, biotite, and most of the sulfides in the potassic and phyllic alteration zones. This means the rutile will record the age of porphyry mineralization. An advantage of LA-ICP-MS rutile U–Pb dating is that it typically contains adequate U and radiogenic Pb for accurate dating (Santos et al., 2020; Schirra and Laurent, 2021). The closure temperature for Pb diffusion in rutile is strongly dependent on the grain size. For a cooling rate of 1 °C Ma^{-1} and spherical geometry, Cherniak (2000) determined closure temperature (T_c) values of 567 °C for 70 μm-size grains and 617 °C for 200 μm-size grains. This T_c is higher than the formation temperature of

353 hydrothermal quartz veins reflected by the homogenization temperatures (T_h)
354 of fluid inclusions (~500–600 °C in the EB and A veins, and ~375–500 °C in
355 the B veins; Sun et al., 2021). Consequently, rutile fulfills the basic
356 requirements for a reliable U-Pb geochronometer. The U-Pb dating of
357 hydrothermal rutile should yield the crystallization ages and the timing of given
358 hydrothermal mineralization, instead of representing cooling ages.

359 In this study, *in situ* U-Pb dating of the rutile yields a lower intercept age
360 of 41.8 ± 1.2 Ma (Fig. 8c), which overlaps the previously reported molybdenite
361 Re-Os ages (Fig. 8d). Significant scatter and abnormal MSWD values of the
362 rutile U-Pb data within a single sample could be due to multiple preserved
363 generations of rutile (Fig. 8a–b). Furthermore, the common Pb incorporation
364 in rutile grains could also result in over-dispersion without a requirement for
365 multiple rutile populations (e.g. Plavsa et al., 2018; Santos et al., 2020). This
366 could be accounted for by U-Pb perturbation during dissolution and
367 reprecipitation recrystallization above the T_c for rutile during the early
368 hydrothermal process. Although the internal precision of individual rutile U-Pb
369 weighted mean dates is significantly lower than that of the zircon U-Pb and
370 molybdenite Re-Os, they all overlap within the uncertainty and are not
371 resolvable. This suggests that the bulk of the Yulong Cu-Mo mineralization
372 formed broadly synchronously with the emplacement of the porphyritic
373 monzogranite.

374 **Origin and formation environment of TiO_2 polymorphs**

375 The distinctive textures and compositions of TiO_2 polymorphs replacing
376 Ti-rich minerals during hydrothermal alteration in porphyry Cu(-Mo-Au)
377 deposits may better reflect the mineralization processes. TiO_2 polymorphs in
378 the fine-grained matrix and hydrothermal veins studied coexist with typical
379 hydrothermal biotite, anhydrite, sericite, magnetite, and sulfides (e.g.
380 chalcopyrite, molybdenite, and pyrite indicating a hydrothermal origin (Fig. 3).
381 Likewise, these polymorphs can reflect different temperature and pressure
382 conditions, driven by hydrothermal fluids (Triebold et al., 2011; Plavsa et al.,
383 2018).

384 Anatase and brookite typically form during low temperature and pressure
385 metamorphism and alteration, with aqueous low-T conditions promoting their
386 stability (Smith et al., 2009; Plavsa et al., 2018). The type-I brookite and
387 anatase at Yulong are present in a fine-grained matrix of altered porphyry and
388 commonly pseudomorph magmatic titanite (Fig. 3a–c). This highlights the role
389 of low-temperature hydrothermal fluids in destabilizing primary Ti-bearing
390 minerals during argillic alteration. This interpretation is also confirmed by
391 porphyry hand specimens that are overprinted by strong argillic alteration in
392 the late-stage mineralization (Fig. 2b). Lower temperature polymorphs
393 (anatase and brookite) have systematically different geochemical signatures
394 to rutile. Previous studies have demonstrated that the availability of HFSE and

395 base metals such as V–Cr–W–Fe for inclusion in the brookite and anatase is
396 largely controlled by the breakdown of precursor Ti-rich minerals and co-
397 precipitation of other phases (Triebold et al., 2011; Plavsa et al., 2018).

398 Rutile associated with porphyry copper deposits forms at temperatures
399 between ~400 and 700 °C, pressures of a few hundred MPa, fO_2 above the
400 nickel-nickel oxide (NNO) buffer, and under hydrous conditions (Rabbia and
401 Hernández, 2012). A hydrothermal fluid associated with the overall
402 development of a porphyry deposit does not have a consistent temperature,
403 fO_2, pH, and chlorine content, and such fluids interact with the ore-bearing
404 porphyry (Rabbia and Hernández, 2012). The presence of rutile crystallizing
405 during hydrothermal alteration can be interpreted as representing localized re-
406 equilibration and breakdown of Ti-rich minerals, such as titanite, biotite, and
407 ilmenite (Scott, 2005; Rabbia et al., 2009).

408 The chemical stability of pre-existing Ti-rich minerals is extremely
409 susceptible to high-temperature and SO_2-rich oxidizing fluids, which could
410 explain why rutile is present in zones of hydrothermal alteration in porphyry
411 deposits (Rabbia and Hernández, 2012). Fluids metasomatism promoted the
412 incomplete replacement of the earlier titanite by type-II rutile in the early
413 hydrothermal quartz A veins (e.g. titanite + SO_2-rich fluid → anhydrite + quartz
414 + rutile), which also records the breakdown of Ti-rich minerals during the
415 introduction of high-temperature fluids (Fig. 3d–f).

In contrast to titanite and ilmenite, Ti-rich magmatic biotite and hornblende initially re-equilibrate to hydrothermal biotite during K-alteration (e.g. Rabbia and Hernández, 2012; Mercer and Reed, 2013; Xiao et al., 2021). The breakdown of Ti-rich biotite is regarded as the main mechanism generating hydrothermal rutile associated with veins developed during widespread K-alteration in the Yulong deposit (Fig. 3g–h). Under a subsequent moderate temperature of 300–400 ºC at elevated fO_2 levels during phyllic alteration, hydrothermal magnetite becomes unstable and is completely replaced by hematite intergrown with hydrothermal rutile (Fig. 3i). The relatively high Ti concentration (1.16-2.68 wt%) of hydrothermal biotite at Yulong makes it a potential source for rutile. Additionally, the intergrowth relationships between individual, blocky type-III rutile and Cu-Fe sulfides in hydrothermal veins (i.e. B veins; Fig. 3j–o), support the conclusion that rutile is a product of precipitation from aqueous fluids as a vein-filling phase indicative of Ti migration. A similar relationship of rutile forming synchronously with Cu-Mo mineralization has been reported for deposits such as Batu Hijau, Bingham Canyon, El Salvador, and North Parkes (Schirra and Laurent, 2021).

The composition of hydrothermal fluid is another factor controlling the growth of rutile (Rabbia and Hernández, 2012; Schirra and Laurent, 2021). Recent experimental work on high temperature metamorphic rocks demonstrates that the solubility of rutile increases significantly in F- and Cl^--

437 rich brines (Rapp et al., 2010). Apatite is known to preferentially incorporate F
438 and apatite inclusions are widely recognized in various stages of hydrothermal
439 veins at Yulong (Fig. 4b; Chang et al., 2018). Once the precipitation of apatite
440 took place, the mineralizing fluids became depleted in F, consequently
441 reducing the solubility of Ti, Zr and other HFSE resulting in Ti saturation and
442 the crystallization of rutile. In addition, unlike the slow heating and cooling
443 processes in metamorphic rocks, hydrothermal rutile is commonly formed in
444 events with rapid pulsating fluid flow leading to enrichment of Zr (Cabral et al.,
445 2015; Agangi et al., 2019; Feng et al., 2020). The estimated rutile
446 crystallization temperature in this study using the Zr-in-rutile thermometer of
447 Tomkins et al. (2007) is over 100 °C higher than the fluid inclusion
448 temperature reported by Sun et al. (2021) demonstrating that Zr-in-rutile
449 thermometer is not appropriate for use in rutile of hydrothermal origin (Cabral
450 et al., 2015). Thus, the origin of rutile in hydrothermal veins might be due to
451 the effect of fluorine (i.e. fluorapatite) on the solubility of rutile.

452 **Introduction of W in the hydrothermal rutile**

453 The composition of hydrothermal rutile in this study has wide variations in
454 the concentrations of Fe, V, Nb, and W (Fig. 6f). Consequently, a single-spot
455 analysis may not be representative of the bulk composition of rutile grains,
456 similar to what was seen by Meinhold (2010). Combining BSE images with
457 element mapping of rutile grains can reveal complex zonation patterns or

458 patchy zoned crystals. Our analyses of rutile crystals show that W content
459 correlates positively with BSE brightness (Figs. 7 and 9), and the patchy or
460 sector zonation is controlled by the distribution of trace elements in rutile.

461 The chemical structure of rutile consists of chains of TiO_6^{8-} octahedra that
462 link each oxygen in triangular coordination with Ti^{4+} ions (Baur, 2007; Klein
463 and Dutrow, 2007). It has been found in previous studies that Ti in the rutile
464 crystal lattice can be substituted by W, Fe, V and Nb, and the substitution of
465 Ti^{4+} is controlled by the ionic radius and ionic charge of the substituted cation
466 (Meinhold, 2010; Win et al., 2017; Reznitsky et al., 2017; Agangi et al., 2019,
467 2020; Adlakha et al., 2020).

468 The oxidation state of Fe, V, Nb, Cr, and W in rutile of this study and their
469 substitution mechanisms are evaluated using binary plots (Fig. 11). The cation
470 percentages were calculated using the number of total cations for oxygen
471 being 2, and iron predominantly being incorporated into rutile as Fe^{3+} (Murad
472 et al., 1995; Bromiley et al., 2004; Win et al., 2017). The M^{3+} represents the
473 trivalent cations (i.e. Fe^{3+}, Cr^{3+}, and V^{3+}). The slope of Ti and V range from -1
474 to -1/3, reflecting the equation $V^{3+} + M^{5+} \leftrightarrow 2Ti^{4+}$ in the W-poor rutile and $2V^{3+}$
475 $+ W^{6+} \leftrightarrow 3Ti^{4+}$ in the W-rich rutile, but the direct substitution of V^{4+} for Ti^{4+} is
476 rare (Fig. 11a). The partial trivalent elements Fe, Cr, and V for the W-poor
477 rutile, and the Nb content of rutile containing M^{3+} exhibit a slope > 1 (Fig. 11b),
478 reflecting the compatibility of different valences (i.e. V^{5+}, or Fe^{2+}) in rutile. The

This is the peer-reviewed, final accepted version for American Mineralogist, published by the Mineralogical Society of America.
The published version is subject to change. Cite as Authors (Year) Title. American Mineralogist, in press.
DOI: https://doi.org/10.2138/am-2022-8453. http://www.minsocam.org/

correlation between the M^{3+} and W^{6+} in the W-rich rutile corresponds to a slope of 2 (Fig. 11c), indicating coupled substitutions with a strong correlation following the chemical equation $2M^{3+} + W^{6+} \leftrightarrow 3Ti^{4+}$. The correlation between W and Fe in the W-rich rutile (slope = 2; Fig. 11d), is consistent with the equation $2Fe^{3+} + W^{6+} \leftrightarrow 3Ti^{4+}$. A strong negative correlation between Ti and $W^{6+} + 2M^{3+}$ in the W-rich rutile grains (slope = -1.02, R^2 = 0.98) clearly shows that W incorporated into the hydrothermal rutile is largely controlled by the reaction $2M^{3+} + W^{6+} \leftrightarrow 3Ti^{4+}$ (Fig. 11e). Based on the correlations between Ti and $Nb^{5+} + 2M^{3+}$ of the W-poor rutile (slope = -1.03, R^2 = 0.88; Fig. 11f), Nb^{5+} might substitute into the rutile lattice structure following the similar reaction $M^{3+} + Nb^{5+} \leftrightarrow 2Ti^{4+}$. In addition, many rutile grains contain high concentrations of Fe, Cr, and V relative to Nb or W, as the data trends plot above the correlation line without intersecting 0 (Fig. 11a, c). This is explained by excess amounts of Fe^{3+}, Cr^{3+}, and V^{4+} substituting for Ti^{4+} in rutile.

Alternatively, the possibility of vacancy-bearing substitutions has been proposed, with hydrogen atoms or OH groups being involved in local charge compensation at the oxygen position in rutile and cassiterite samples (Maldener et al., 2001; Losos and Beran, 2004; Borges et al., 2015). However, recent Raman and X-ray absorption spectroscopy studies of W-rich rutile exclude the possibility of hydrogen acting as a charge balancing species or

499 oxygen vacancies (Majzlan et al., 2021). These suppositions are also not
500 supported by analyses completed in this study.

501 Another parameter that favors substitution of Ti by W is the similarity in
502 their ionic radii (Shannon, 1976). Under the condition of charge balance, the
503 virtually identical ionic radius in sixfold coordination of W^{6+} (0.74 Å) is
504 arguably favorable for the replacement of Ti^{4+} (0.745 Å) in the rutile crystal
505 structure. In addition to these mechanisms, non-equilibrium incorporation of
506 trace elements during fast mineral growth in hydrothermal ore systems
507 (Agangi et al., 2019) cannot be ignored.

508 **Source of W and hydrothermal fluid signatures in the Yulong porphyry**
509 **Cu-Mo deposit**

510 Previous studies show that the presence of pathfinder elements such as
511 W, Nb, V, Sn, and Fe in hydrothermal rutile is influenced by the nature of
512 precursor minerals and the composition of magmatic or metamorphic fluids
513 (Plavsa et al., 2018; Agangi et al., 2020; Schirra and Laurent, 2021). Rutile at
514 Yulong contains high levels of W, V, Fe, and Nb (Fig. 10), similar to rutile from
515 other porphyry deposits (Scott, 2005; Rabbia et al., 2009; Mercer and Reed,
516 2013; Schirra and Laurent, 2021). We therefore interpret the chemical
517 composition of rutile formed in a hydrothermal ore system to reflect the
518 composition of ore-forming fluids associated with porphyry Cu-Mo
519 mineralization.

520 The crystallographic control of impurities into the rutile lattice during
521 crystal growth can cause compositional variations such as sector zoning
522 (Plavsa et al., 2018; Agangi et al., 2020; Moore et al., 2020; Majzlan et al.,
523 2021). The intensity of backscattered luminescence is related to the relative
524 atomic mass of elements. Due to the common presence of elements such as
525 W, Nb, V and Fe heavier than Ti, the incorporation of trace elements results in
526 brighter sectors in BSE images. In this study, hydrothermal rutile preserves
527 well-developed patchy and sector zoning (Fig. 9a–b), which largely relates to
528 the contribution of W (Fig. 9c). However, the element mapping of residual
529 titanite that is incompletely replaced by rutile in the quartz veins shows
530 extremely low W content (Fig. 7a), indicating that W is unlikely inherited from
531 primary Ti-rich minerals. In general, several HFSEs such as W, Nb, and V
532 form complexes with F in aqueous fluids. These elements tend to be enriched
533 in rocks formed from strongly fractionated, typically F-rich and high-Cl felsic
534 magmatic-hydrothermal fluids (Carruzzo et al., 2006; Chevychelov et al., 2005;
535 Agangi et al., 2020). The presence of F-bearing phases in the minerals
536 studied such as fluorapatite (e.g. average 3.13 wt% F; Huang et al., 2019),
537 indicates the presence of F in the mineralizing fluids, explaining the
538 mobilization of HFSEs (Fig. 12). The latest studies of the composition of fluid
539 inclusions, using LA-ICP-MS, confirm that brine and intermediate density
540 inclusions in the early- and transitional-stage quartz veins represent the main

mineralization event at Yulong. The inclusions contain W assaying up to thousands of ppm (Chang et al., 2018). Furthermore, the presence of high valence cations also points towards high fO_2 during the hydrothermal alteration in the porphyritic monzogranite at Yulong, which is further supported by the presence of texturally associated anhydrite (Fig. 4c).

Deciphering the signatures of ore-forming fluids is a prerequisite in deciphering the genesis of mineral deposits (Cao et al., 2020; Qiu et al., 2021). The brookite and anatase in the fine-grained matrix of altered porphyritic monzogranite, and forming pseudomorphs after magmatic titanite and at contacts with monazite, magnetite, and quartz, indicating that the lower temperature argillic alteration associated with late-stage mineralization was in an H_2O-rich environment with a relatively high fO_2 (Broska et al. 2007; Huang et al., 2019; Xiao et al., 2021). This easily overlooked observation suggests that TiO_2 polymorphs can be produced by varying degrees of hydrothermal fluids modification in a porphyry system (Plavsa et al., 2018). The texture and geochemistry of the type-II rutile indicate that the hydrothermal fluid during potassic alteration was more oxidized, preceding the main mineralization stage. The widespread occurrence of the type-III rutile intergrown with sulfides formed during the main mineralization stage shows that Ti can be highly mobile in hydrothermal fluids during porphyry alteration. Furthermore, the enrichment of W in the type-III rutile indicates that these elements are highly

562 mobile in the hydrothermal fluids in the presence of halogen-rich (F, Cl)
563 aqueous fluids associated with the mineralization at Yulong.

564 In summary, the mineralizing hydrothermal fluids in the Yulong deposit
565 had a high fO_2 at a high-temperature, and were rich in SO_2 and F. This
566 resulted in the breakdown of pre-existing Ti-rich minerals and mobilizing
567 relatively insoluble HFSEs. These ore-forming fluids are crucial for the
568 formation of hydrothermal rutile in porphyry deposits.

569

570 **Implications**

571 The textures, assemblages, and compositions of hydrothermal rutile
572 forming contemporaneously with ore mineralization can provide clues and
573 information regarding the genesis of hydrothermal processes during the
574 growth of magmatic-hydrothermal deposits. The trace element composition of
575 hydrothermal rutile can be used as a pathfinder for hydrothermal activity. The
576 introduction of trace elements driven by hydrothermal alteration explains the
577 variety of chemical compositions observed in natural hydrothermal rutile found
578 in porphyry copper deposits. High-temperature ore-forming fluids with high
579 oxygen fugacity, and rich in SO_2 and F can promote the introduction of
580 relatively insoluble high field-strength elements and base metals (such as W)
581 into the crystal lattice of rutile. Consequently, the chemical or isotopic
582 composition recorded in rutile provides comprehensive information allowing

583 us to better understand the nature of hydrothermal fluids operating during the
584 deposition of porphyry deposits. This in turn potentially allows us to define
585 vectors towards the location of porphyry deposits. Geochemistry of
586 hydrothermal rutile can be expected to provide additional insights into
587 hydrothermal fluid compositions responsible for different mineralization styles.
588 In addition, it has been identified that anatase and brookite (rather than rutile)
589 replaced titanite during low temperature argillic alteration. Thus, detailed and
590 correct identification of TiO_2 polymorphs may much better understand
591 hydrothermal processes, particularly during using rutile geochemistry as a
592 vector towards mineralisation.
593

594 **Acknowledgments**

595 This work was supported by the National Key Research and
596 Development Project of China (Number 2020YFA0714802), the National
597 Natural Science Foundation of China (Numbers 41872080), and the Most
598 Special Fund from the State Key Laboratory of Geological Processes and
599 Mineral Resources in China University of Geosciences (Beijing) of China
600 (Number MSFGPMR201804). We are grateful to Shentai Liu, the Engineer of
601 Tibet Yulong Copper Co, Ltd, for his assistance during the field investigation.
602 We thank Diana Zivak, University of Adelaide, Australia, and the anonymous
603 journal reviewers for their critical reviews and constructive comments. We are

also grateful to the Editor Prof. Hongwu Xu and Associate Editor Prof. Paul Tomascak for their valuable help in handling this paper.

References cited

Adlakha, E.E., Hattori, K., Kerr, Mitchell. J., and Boucher, B.M. (2020). The origin of Ti-oxide minerals below and within the eastern Athabasca Basin, Canada. American Mineralogist, 105, 1875–1888.

Agangi, A., Plavsa, D., Reddy, S.M., Olierook, H., and Kylander-Clark, A. (2020) Compositional modification and trace element decoupling in rutile: Insight from the Capricorn Orogen, western Australia. Precambrian Research, 345, 105772.

Agangi, A., Reddy, S.M., Plavsa, D., Fougerouse, D., Clark, C., Roberts, M., and Johnson, T.E. (2019) Antimony in rutile as a pathfinder for orogenic gold deposits. Ore Geology Reviews, 106, 1–11.

Baur, W.H. (2007) The rutile type and its derivatives. Crystallography Reviews 13, 65–113.

Borges, P.D., Scolfaro, L., and Assali, L.V.C. (2015) Complex centers of hydrogen in tin dioxide. Theoretical Chemistry Accounts, 134, article 131.

Bromiley, G.D., Hilairet, N., and McCammon, C. (2004) Solubility of hydrogen and ferric iron in rutile and TiO2 (II): implications for phase

625 assemblages during ultra-high pressure metamorphism and for the
626 stability of silica polymorphs in the lower mantle. Geophysical
627 Research Letters, 31, LO4610.
628 Broska, I., Harlov, D., Tropper, P., and Siman, P. (2007) Formation of
629 magmatic titanite and titanite–ilmenite phase relations during granite
630 alteration in the Tribeč Mountains, Western Carpathians, Slovakia.
631 Lithos, 95, 58–71.
632 Cabral, A.R., Rios, F.J., de Oliveira, L.A.R., de Abreu, F.R., Lehmann, B.,
633 Zack, T., and Laufek, F. (2015) Fluid-inclusion microthermometry and
634 the Zr-in-rutile thermometer for hydrothermal rutile. International
635 Journal of Earth Sciences, 104, 513–519.
636 Cao, M.J., Hollings, P., Evans, N.J., Cooke, D.R., McInnes, B.I.A., Zhao, K.D.,
637 Qin, K.Z., Li, D.F., and Sweet, G. (2020) In situ elemental and Sr
638 isotopic characteristics of magmatic to hydrothermal minerals from the
639 Black Mountain porphyry deposit, Baguio district, Philippines.
640 Economic Geology, 115, 927–944.
641 Carruzzo, S., Clarke, D.B., Pelrine, K.M., and MacDonald, M.A. (2006)
642 Texture, composition, and origin of rutile in the South Mountain
643 Batholith, Nova Scotia. Canadian Mineralogist, 44, 715–729.
644 Chang, J., Li, J.W., and Audétat, A. (2018) Formation and evolution of
645 multistage magmatic-hydrothermal fluids at the Yulong porphyry Cu-Mo

646 deposit, eastern Tibet: Insights from LA-ICP-MS analysis of fluid
647 inclusions. Geochimica et Cosmochimica Acta, 232, 181–205.
648 Chang, J., Li, J.W., Selby, D., Liu, J.C., and Deng, X.D. (2017) Geological and
649 chronological constraints on the long-lived Eocene Yulong porphyry
650 Cu-Mo deposit, eastern Tibet, China: Implications for lifespan of
651 magmatic-hydrothermal processes forming giant and supergiant
652 porphyry Cu deposits. Economic Geology, 112, 1719–1746.
653 Chen, Q., Wang C.M., Bagas, L., Zhang, Z.C., and Du, B. (2021) Time scales
654 of multistage magma-related hydrothermal fluids at the giant Yulong
655 porphyry Cu-Mo deposit in eastern Tibet: Insights from titanium
656 diffusion in quartz. Ore Geology Reviews, 139(A), 104459.
657 doi.org/10.1016/j.oregeorev.2021.104459
658 Cherniak, D.J. (2000) Pb diffusion in rutile. Contributions to Mineralogy and
659 Petrology, 139, 198–207.
660 Chevychelov, V.Y., Zaraisky, G.P., Borisovskii, S.E., and Borkov, D.A. (2005)
661 Effect of melt composition and temperature on the partitioning of Ta,
662 Nb, Mn, and F between granitic (alkaline) melt and fluorine-bearing
663 aqueous fluid: fractionation of Ta and Nb and conditions of ore
664 formation in rare-metal granites. Petrology, 13, 305–321.

665 Chiaradia, M., Schaltegger, U., and Spikings, R. (2014) Time scales of
666 mineral systems—advances in understanding over the past decade.
667 Society of Economic Geologists, Special Publication 18, 37–58.
668 Clark, J.R., and Williams-Jones, A.E. (2004) Rutile as a potential indicator
669 mineral for metamorphosed metallic ore deposits, Rapport Final de
670 DIVEX, Sous-projet SC2: Montreal, p. 17.
671 Czamanske, G.K., Force, E.R., and Moore, W.J., 1981. Some geologic and
672 potential resource aspects of rutile in porphyry copper deposits.
673 Economic Geology, 76, 2240–2256.
674 Deng, J., Wang, C.M., Bagas, L., Selvaraja, V., Jeon, H., Wu, B., and Yang,
675 L.F. (2017) Insights into ore genesis of the Jinding Zn-Pb deposit,
676 Yunnan Province, China: Evidence from Zn and in situ S isotopes. Ore
677 Geology Reviews, 90, 943–957.
678 Deng, J., Wang, C.M., Zi, J.W., Xia, R., and Li, Q. (2018) Constraining
679 subduction-collision processes of the Paleo-Tethys along The
680 Changning-Menglian Suture: New zircon U-Pb ages and Sr-Nd-Pb-Hf-
681 O isotopes of the Lincang Batholith. Gondwana Research, 62, 75–92.
682 Ewing, T.A., Hermann, J., and Rubatto, D. (2013) The robustness of the Zr-in-
683 rutile and Ti-in-zircon thermometers during high-temperature
684 metamorphism (Ivrea-Verbano Zone, northern Italy). Contributions to
685 Mineralogy and Petrology, 165, 757–779.

686 Feng, H.X., Shen, P., Zhu, R.X., Ma, G., and Li, J.P. (2020) SIMS U-Pb dating
687 of vein-hosted hydrothermal rutile and carbon isotope of fluids in the
688 Wulong lode gold deposit, NE China: Linking gold mineralization with
689 craton destruction. Ore Geology Reviews, 127, 103838.
690 doi.org/10.1016/j.oregeorev.2020.103838
691 Gao, X.Y., Zheng, Y.F., Xia, X.P., and Chen, Y.X. (2014) U-Pb ages and trace
692 elements of metamorphic rutile from ultrahigh-pressure quartzite in the
693 Sulu orogeny. Geochimica et Cosmochimica Acta, 143, 87–114.
694 Hart, E., Storey, C., Harley, S.L., and Fowler, M. (2018) A window into the
695 lower crust: trace element systematics and the occurrence of
696 inclusions/intergrowths in granulite-facies rutile. Gondwana Research,
697 59, 76–86.
698 Hou, Z.Q., Ma, H.W., Khin, Z., Zhang, Y.Q., Wang, M.J., Wang, Z., Pan, G.T.,
699 and Tang, R.L. (2003) The Himalayan Yulong porphyry copper belt:
700 Product of large-scale strike-slip faulting in eastern Tibet. Economic
701 Geology, 98, 125–145.
702 Hou, Z.Q., Yang, Z.M., Lu, Y.J., Kemp, A., Zheng, Y.C., Li, Q.Y., Tang, J.X.,
703 Yang, Z.S., and Duan, L.F. (2015) A genetic linkage between
704 subduction- and collision-related porphyry Cu deposits in continental
705 collision zones. Geology, 43, 247–250.

706 Hou, Z.Q., Zeng, P.S., Gao, Y.F., Du, A.D., and Fu, D.M. (2006) Himalayan
707 Cu–Mo–Au mineralization in the eastern Indo-Asian collision zone:
708 constraints from Re–Os dating of molybdenite. Mineralium Deposita,
709 41, 33–45
710 Huang, M.L., Bi, X.W., Richards, J.P., Hu, R.Z., Xu, L.L., Gao, J.F., Zhu, J.J.,
711 and Zhang, X.C. (2019) High water contents of magmas and extensive
712 fluid exsolution during the formation of the Yulong porphyry Cu-Mo
713 deposit, eastern Tibet. Journal of Asian Earth Sciences, 176, 168–183.
714 Klein, C., and Dutrow, B. (2007) Manual of Mineral Science, 23rd ed. 716 p.
715 Wiley, New Jersey.
716 Li, J.X., Qin, K.Z., Li, G.M., Cao, M.J., Xiao, B., Chen, L., Zhao, J.X., Evans,
717 N.J., and McInnes, B.I.A. (2012) Petrogenesis and thermal history of
718 the Yulong porphyry copper deposit, Eastern Tibet: insights from U-Pb
719 and U-Th/He dating, and zircon Hf isotope and trace element analysis.
720 Mineralogy and Petrology, 105, 201–221.
721 Liang, H.Y., Campbell, I.H., Allen, C., Sun, W.D., Liu, C.Q., Yu, H.X., Xie,
722 Y.W., and Zhang, Y.Q. (2006) Zircon Ce^{4+}/Ce^{3+} ratios and ages for
723 Yulong ore-bearing porphyries in eastern Tibet. Mineralium Deposita,
724 41, 152–159.
725 Losos, Z., and Beran, A. (2004) OH defects in cassiterite. Mineralogy and
726 Petrology, 81, 219–234.

727 Lu, Y.J., Loucks, R.B., Fiorentini, M.L., Yang, Z.M., and Hou, Z.Q. (2015)
728 Fluid flux melting generated post-collisional high-Sr/Y copper ore-
729 forming water-rich magmas in Tibet. Geology, 43, 583–586.
730 Ludwig, K.R. (2008) A User's Manual for Isoplot 3.6: A Geochronological
731 Toolkit for Microsoft Excel. Berkeley Geochronological Center
732 Luvizotto, G.L., and Zack, T. (2009) Nb and Zr behavior in rutile during high-
733 grade metamorphism and retrogression: an example from the Ivrea-
734 Verbano Zone. Chemical Geology, 261, 303–317.
735 Majzlan, J., Bolanz, R., Göttlicher, J., Mikuš, T., Milovská, S., Čaplovičová, M.,
736 Števko, M., Rössler, C., and Matthes, C. (2021) Incorporation
737 mechanism of tungsten in W-Fe-Cr-V-bearing rutile. American
738 Mineralogist, 106(4), 609–619.
739 Maldener, J., Rauch, F., Gavranic, M., and Beran, A. (2001) OH absorption
740 coefficients of rutile and cassiterite deduced from nuclear reaction
741 analysis and FTIR spectroscopy. Mineralogy and Petrology, 71, 21–29.
742 Meinhold, G. (2010) Rutile and its applications in earth sciences. Earth-
743 Science Reviews, 102, 1–28.
744 Mercer, C.N., and Reed, M.H. (2013) Porphyry Cu-Mo stockwork formation by
745 dynamic, transient hydrothermal pulses: Mineralogic insights from the
746 deposit at Butte, Montana. Economic Geology, 108, 1347–1377.

747 Meyer, M., John, T., Brandt, S., and Klemd, R. (2011) Trace element
748 composition of rutile and the application of Zr-in-rutile thermometry to
749 UHT metamorphism (Europa complex, NW Namibia). Lithos, 126, 388–
750 401.
751 Moore, J., Beinlich, A., Porter, J.K., Talavera, C., Berndt, J., Piazolo, S.,
752 Austrheim, H., and Putnis, A. (2020). Microstructurally controlled trace
753 element (Zr, U–Pb) concentrations in metamorphic rutile: An example
754 from the amphibolites of the Bergen Arcs. Journal of Metamorphic
755 Geology, 38, 103–127.
756 Murad, E., Cashion, J.D., Noble, C.J., and Pilbrow, J.R. (1995) The chemical
757 state of Fe in rutile from an albitite in Norway. Mineralogical Magazine,
758 59, 557–560.
759 Okay, N., Zack, T., Okay, A.I., and Barth, M. (2011) Sinistral transport along
760 the Trans-European Suture Zone: detrital zircon-rutile geochronology
761 and sandstone petrography from the Carboniferous flysch of the
762 Pontides. Geological Magazine, 148, 380–403.
763 Paton, C., Hellstrom, J., Paul, B., Woodhead, J., and Hergt, J. (2011) Iolite:
764 freeware for the visualization and processing of mass spectrometric
765 data. Journal of Analytical Atomic Spectrometry, 26, 2508–2518.
766 Pe-Piper, G., Nagle, J., Piper, D., and Mcfarlane, C. (2019) Geochronology
767 and trace element mobility in rutile from a Carboniferous syenite

768 pegmatite and the role of halogens. American Mineralogist, 104, 501–
769 513.
770 Pereira, I., Storey, C., Darling, J., Lana, C., and Alkmim, A.R. (2019) Two
771 billion years of evolution enclosed in hydrothermal rutile: Recycling of
772 the São Francisco Craton Crust and constraints on gold remobilisation
773 processes. Gondwana Research, 68, 69–92.
774 Pi, Q.H., Hu, R.Z., Xiong, B., Li, Q.L., and Zhong, R.C. (2017) In situ SIMS U-
775 Pb dating of hydrothermal rutile: reliable age for the Zhesang Carlin-
776 type gold deposit in the golden triangle region, SW China. Mineralium
777 Deposita, 52, 1179–1190.
778 Plavsa, D., Reddy, S.M., Agangi, A., Clark, C., Kylander-Clark, A., and Tiddy,
779 C.J. (2018) Microstructural, trace element and geochronological
780 characterization of TiO_2 polymorphs and implications for mineral
781 exploration. Chemical Geology, 476, 130–149.
782 Qiu, K.F., Yu, H.C., Hetherington, C., Huang, Y.Q., Yang, T., and Deng, J.
783 (2021) Tourmaline composition and boron isotope signature as a tracer
784 of magmatic-hydrothermal processes. American Mineralogist, 106,
785 1033–1044.
786 Rabbia, O., and Hernández, L.B. (2012) Mineral chemistry and potential
787 applications of natural-multi-doped hydrothermal rutile from porphyry

copper deposits. In I. M. Low, Eds., Rutile: Properties, Synthesis and Application, Nova Science Publishers, p. 209–228.

Rabbia, O.M., Hernández, L.B., French, D.H., King, R.W., and Ayers, J.C. (2009) The El Teniente porphyry Cu–Mo deposit from a hydrothermal rutile perspective. Mineralium Deposita, 44, 849–866.

Rapp, J.F., Klemme, S., Butler, I.B., and Harley, S.L. (2010) Extremely high solubility of rutile in chloride and fluoride-bearing metamorphic fluids: an experimental investigation. Geology, 38, 323–326.

Reznitsky, L.Z., Sklyarov, E.V., Suvorova, L.F., Barash, I.G., and Karmanov, N.S. (2017) V-Cr-Nb-W-bearing rutile in metamorphic rocks of the Slyudyanka complex, southern Baikal region. Geology of Ore Deposits, 59, 707–719.

Rösel, D., Zack, T., and Moller, A. (2019) Interpretation and significance of combined trace element and U-Pb isotopic data of detrital rutile: a case study from late Ordovician sedimentary rocks of Saxo-Thuringia, Germany. International Journal of Earth Sciences, 108, 1–25.

Santos, M.M., Lana, C., Scholz, R., Buick, I.S., Kamo, S.L., Corfu, F., and Queiroga, G. (2020) LA-ICP-MS U-Pb dating of rutiles associated with hydrothermal mineralization along the southern Araçuaí Belt, SE Brazil. Journal of Asian Earth Sciences, 99, 1–15.

808 Schirra, M., and Laurent, O. (2021) Petrochronology of hydrothermal rutile in
809 mineralized porphyry Cu systems. Chemical Geology, 581, 120407.
810 doi.org/10.1016/j.chemgeo.2021.120407
811 Scott, K.M. (2005) Rutile geochemistry as a guide to porphyry Cu-Au
812 mineralization, North Parkes, New South Wales, Australia.
813 Geochemistry: Exploration, Environment, Analysis, 5, 247–253.
814 Scott, K.M., Radford, N.W., Hough, R.M., Reddy, S.M. (2011) Rutile
815 compositions in the Kalgoorlie Goldfields and their implications for
816 exploration. Australian Journal of Earth Sciences, 58, 803–812.
817 Sengün, F., and Zack, T. (2016) Trace element composition of rutile and Zr-
818 in-rutile thermometry in meta-ophiolitic rocks from the Kazdağ Massif,
819 NW Turkey. Mineralogy and Petrology, 110, 547–560.
820 Şengün, F., Zack, T., and Dunklc, I. (2020) Provenance of detrital rutiles from
821 the Jurassic sandstones in the Central Sakarya Zone, NW Turkey: U-
822 Pb ages and trace element geochemistry. Geochemistry, 80, 125667.
823 doi.org/10.1016/j.chemer.2020.125667
824 Shannon, R.D. (1976) Revised effective ionic radii and systematic studies of
825 interatomic distances in halides and chalcogenides. Acta
826 Crystallographica, A32, 751–767.
827 Smith, S.J., Stevens, R., Liu, S.F., Li, G.S., Navrotsky, A., Boerio-Goates, J.,
828 and Woodfield, B.F. (2009) Heat capacities and thermodynamic

functions of TiO_2 anatase and rutile: analysis of phase stability. American Mineralogist, 94 (2–3), 236–243.

Sun, M.Y., Monecke, T., Reynolds, T.J., and Yang, Z.M. (2021) Understanding the evolution of magmatic-hydrothermal systems based on microtextural relationships, fluid inclusion petrography, and quartz solubility constraints: insights into the formation of the Yulong Cu-Mo porphyry deposit, eastern Tibetan Plateau, China. Mineralium Deposita, 56, 823–842.

Tang, R.L., and Luo, H.S. (1995) The geology of Yulong porphyry copper (molybdenum) ore belt, Xizang (Tibet), 1–320 p. Geological Publishing House, Beijing.

Tomkins, H.S., Powell, R., and Ellis, D.J. (2007) The pressure dependence of the zirconium-in-rutile thermometer. Journal of Metamorphic Geology, 25, 703–713.

Triebold, S., Luvizotto, G.L., Tolosana-Delgado, R., Zack, T., and von Eynatten, H. (2011) Discrimination of TiO_2 polymorphs in sedimentary and metamorphic rocks. Contributions to Mineralogy and Petrology, 161, 581–596.

Ver Hoeve, T.J., Scoates, J.S., Wall, C.J., Weis, D., and Amini, M. (2018) A temperature composition framework for crystallization of fractionated interstitial melt in the Bushveld complex from trace element

characteristics of zircon and rutile. Journal Of Petrology, 59, 1383–1416.

Wang, C.H., Tang, J.X., Chen, J.P., Hao, J.H., Gao, Y.M., Liu, Y.W., Fan, T., Zhang, Q.Z., Ying, L.J., and Chen, Z.J. (2009) Chronological research of Yulong copper-molybdenum porphyry deposit. Acta Geologica Sinica, 83, 1445–1455 (In Chinese with English abstract).

Wang, C.M., Bagas, L., Chen, J.Y., Yang, L.F., Zhang, D., Du, B., and Shi, K.X. (2018a) The genesis of the Liancheng Cu-Mo deposit in the Lanping Basin of SW China: Constraints from geology, fluid inclusions, and Cu-S-H-O isotopes. Ore Geology Reviews, 92, 113–128.

Wang, C.M., Bagas, L., Lu, Y.J., Santosh, M., Du, B., and Campbell, M.T. (2016) Terrane boundary and spatio-temporal distribution of ore deposits in the Sanjiang Tethyan Orogen: Insights from zircon Hf-isotopic mapping. Earth-Science Reviews, 156, 39–65.

Wang, C.M., Deng, J., Carranza, E.J.M., and Santosh, M. (2014) Tin metallogenesis associated with granitoids in the southwestern Sanjiang Tethyan Domain: Nature, deposit types, and tectonic setting. Gondwana Research, 26, 576–593.

Wang, C.M., Rao, S.C., Shi, K.X., Bagas, L., Chen, Q., Zhu, J.X., Duan, H.Y., Liu, L.J. (2021) Rutile in Amphibolite Facies Metamorphic Rocks: A

Rare Example from the East Qinling Orogen, China. Applied Sciences. 11, 8756. doi.org/10.3390/app11188756.

Wang, R., Weinberg, R.F., Collins, W.J., Richards, J.P., and Zhu, D.C. (2018b) Origin of post-collisional magmas and formation of porphyry Cu deposits in southern Tibet. Earth-Science Reviews, 181, 122–143.

Williams, I.S. (1998) U–Th–Pb geochronology by ion microprobe. In M.A. McKibben, W.C. Shanks, and W.I. Ridley, Eds., Applications of microanalytical techniques to understanding mineralizing processes, Reviews in Economic geology, 7, 35.

Win, M.M., Enami M., Kato, T., and Thu, Y.K. (2017) A mechanism for Nb incorporation in rutile and application of Zr-in-rutile thermometry: A case study from granulite facies paragneisses of the Mogok metamorphic belt, Myanmar. Mineralogical Magazine, 81, 1503–1521.

Xiao, X., Zhou, T.F., White, N.C., Zhang, L.J., Fan, Y., Chen, X.F. (2021) Multiple generations of titanites and their geochemical characteristics record the magmatic-hydrothermal processes and timing of the Dongguashan porphyry-skarn Cu-Au system, Tongling district, Eastern China. Mineralium Deposita, 56, 363–380.

Yang, Z.M., and Cooke, D.R. (2019) Porphyry copper deposits in China. In Z.S. Chang, R.J. Goldfarb, Eds., Mineral deposits of China, p. 133–187. Society of Economic Geologists, Special Publication, the US.

Yang, Z.M., Hou, Z.Q., Xu, J.F., Bian, X.F., Wang, G.R., Yang, Z.S., Tian, S.H., Liu, Y.C., and Wang, Z.L. (2014) Geology and origin of the post-collisional Narigongma porphyry Cu-Mo deposit, southern Qinghai, Tibet. Gondwana Research, 26, 536–556.

Zack, T., and Kooijman, E. (2017) Petrology and geochronology of rutile. Reviews in Mineralogy and Geochemistry, 83, 443–467.

Zack, T., Kronz, A., Foley, S.F., Rivers, T. (2002) Trace element abundances in rutiles from eclogites and associated garnet mica schists. Chemical Geology, 184, 97–122.

Zack, T., Moraes, R., and Kronz, A. (2004) Temperature dependence of Zr in rutile: empirical calibration of a rutile thermometer. Contributions to Mineralogy and Petrology, 148, 471–488.

Zhang, L., Wu, J.L., Tu, J.R., Wu, D., Li, N., Xia, X.P., and Ren, Z.Y. (2020) RMJG Rutile: A new natural reference material for microbeam U-Pb dating and Hf isotopic analysis. Geostandards and Geoanalytical Research, 44, 133–145.

Figure captions

Fig. 1 (a) Simplified tectonic framework of the Sanjiang Orogen and its adjacent areas (modified after Wang et al., 2014); (b) the simplified geological map of the Eocene Yulong porphyry Cu belt (modified after Hou et al., 2003);

912 (c) Geological map of the Yulong deposit (modified after Chang et al., 2018);
913 and (d–e) Distribution and zonation of mineralization based on the logging of
914 drill core along the two cross-sections. The figure shows the SSE-NNW
915 oriented cross-section A-A' parallel to the long axis and the WSW-ENE
916 oriented cross-section B-B' perpendicular to the long axis of the Yulong
917 porphyry (modified after Chang et al., 2017). The colored circles show the
918 locations of samples analyzed for this study. Abbreviations:
919 JASZ=Jinshajiang-Ailaoshan Suture Zone; LSSZ=Longmu Co-Shuanghu
920 Suture Zone; CMSZ=Changning-Menglian Suture Zone; BNSZ=Bangonghu-
921 Nujiang Suture Zone; YZSZ= Yarlung Zangbo Suture Zone.

922 **Fig. 2** Hand specimen photographs of the syn-mineralization porphyritic
923 monzogranite at Yulong showing: (a) porphyritic monzogranite; (b) argillic
924 altered porphyritic monzogranite; (c) early (EB) biotite–quartz veins and
925 quartz–K-feldspar–pyrite–chalcopyrite (A) veins with potassic alteration; and
926 (d) quartz–chalcopyrite–pyrite (B) veins. Abbreviations: Pl = plagioclase, Kfs =
927 K-feldspar, Py = pyrite, Qz = quartz, Bt = biotite, Ccp = chalcopyrite; Mol =
928 molybdenite.

929 **Fig. 3** Representative examples of photomicrographs (transmitted and
930 reflected light) and BSE images of analyzed TiO_2 polymorphs showing: (a–c)
931 type-I brookite and anatase pseudomorphs after titanite in a fine-grained
932 matrix of altered porphyry and contacting with monazite, chalcopyrite,

933 magnetite, and quartz; (d) elongated and prismatic type-II rutile in clusters
934 associated with the alteration; (e, f) type-II rutile coexisting with relict titanite
935 and showing faint zoning; (g–i) type-III rutile hosted by biotite and hematite
936 showing patchy zoning; (j, k) irregular rutile coexisting with molybdenite; (l)
937 anhedral and concentric zoning rutile intergrown with chalcopyrite; (m, n) type-
938 III rutile included in chalcopyrite; and (o) patchy zoning of type-III rutile
939 coexisting with pyrite. The red circles and numbers represent the EMPA spots
940 in rutile, and the blue circles and numbers are marked as the EMPA spots in
941 other minerals. Abbreviations: Ttn = titanite, Mag = magnetite, Kfs = K-
942 feldspar, Rt = rutile, Ant = anatase, Brk = brookite, Hem = hematite, Py =
943 pyrite, Qz = quartz, Bt = biotite, Ccp = chalcopyrite; Mol = molybdenite, Cv =
944 covellite.

945 **Fig. 4** Representative photomicrographs in transmitted light and BSE images
946 showing: (a) rutile associated with quartz, K-feldspar, zircon, and sericite in
947 veins; (b) columnar apatite inclusions widely distributed in veins; (c) rutile
948 coexisting with anhydrite in the vein halo; and (d) magnetite in EB veins.
949 Abbreviations: Qz = quartz, Rt = rutile, Kfs = K-feldspar, Zrn = zircon, Ser =
950 sericite, Mag = magnetite; Anh = anhydrite; Ap = apatite.

951 **Fig. 5** Comparison of Raman spectra between the standard TiO_2 polymorphs
952 (brookite, anatase, and rutile; Meinhold, 2010) from Yulong showing: (a–b)
953 type-I brookite and anatase from sample 18-13B1; (c) type-II rutile from

954 1103B3; and (d) type-III rutile from 1103B4. Raman spectra spots are marked
955 with yellow letters and crosses in Figure 3.

956 **Fig. 6** Concentrations of selected oxides and trace elements in TiO_2
957 polymorphs showing: (a) TiO_2 vs WO_3; (b) TiO_2 vs V_2O_3; (c) Nb_2O_5 vs V_2O_3; (d)
958 V_2O_3 vs WO_3; (e) Box-and-whisker diagram (constructed from spot EMPA
959 images) for oxide concentrations; and (f) V vs Cr plot with 1-, 2-, and 3-σ
960 probability regions for rutile, anatase, and brookite (modified after Triebold et
961 al., 2011).

962 **Fig. 7** EMPA trace element mapping of: (a) type-II rutile; and (b) type-III rutile.
963 The vertical scale represents the EMPA counts per unit area. The high
964 concentrations of trace elements are shown in red, yellow, and green, and the
965 low concentrations are shown as blue, violet, and dark colors.

966 **Fig. 8** Graphs showing: (a–b) BSE image of two representative rutile grains
967 from the Yulong deposit showing the LA-ICP-MS analysis spots and results;
968 (c) LA-ICP-MS rutile U-Pb Tera–Wasserburg diagram for type-III rutile in
969 hydrothermal veins; and (d) the summary of the zircon U-Pb, molybdenite Re-
970 Os, and rutile U-Pb (this study) data for the Yulong porphyry Cu-Mo deposit
971 (Data sources: Chen et al., 2021 and references therein).

972 **Fig. 9** Relationship between W concentrations and BSE intensity. The green
973 and orange arrows show examples of traverses across rutile with different W
974 concentrations. The original W intensity profiles by EMPA mapping are shown

975 in orange curves, smoothed BSE intensity profiles are shown in green curves,
976 and EMPA spots are shown with circles.

977 **Fig. 10** Selected trace element compositions of rutile from Yulong deposit.
978 The background shades indicate the compositional ranges of rutile from
979 metamorphic, igneous and sedimentary environments, and other porphyry
980 deposits reported in the literature (Data sources: Luvizotto and Zack, 2009;
981 Meyer et al., 2011; Okay et al., 2011; Ewing et al., 2013; Gao et al., 2014;
982 Şengün and Zack, 2016; Hart et al., 2018; Plavsa et al., 2018; Ver Hoeve et
983 al., 2018; Rösel et al., 2019; Pereira et al., 2019; Pe-Piper et al., 2019; Agangi
984 et al., 2020; Şengün et al., 2020; Schirra and Laurent, 2021).

985 **Fig. 11** Binary plots of element abundances in rutile using EPMA data
986 recalculated as atomic cation percent: (a) Ti and V; (b) Nb and Fe+Cr+V; (c)
987 W and Fe+Cr+V; (d) W and Fe; (e) Ti and W^{6+}+2(Fe, Cr, V)$^{3+}$; and (f) Ti and
988 (Nb^{5+}, W^{6+})+2(Fe, Cr, V)$^{3+}$. Trendlines rooted are shown representing different
989 substitution mechanisms, and M^{3+} indicates the sum of the trivalent elements.

990 **Fig. 12** Model of rutile formation via replacement of pre-existing Ti-rich
991 minerals. Flow of mineralizing fluids (blue arrows) can mobilize scarcely
992 soluble elements, such as W, V, Nb, as discussed in the text.

993 **Table caption**

994 **Table 1**. TiO_2 polymorphs textural features and assemblages in the Yulong
995 Cu-Mo porphyry deposit.

This is the peer-reviewed, final accepted version for American Mineralogist, published by the Mineralogical Society of America.
The published version is subject to change. Cite as Authors (Year) Title. American Mineralogist, in press.
DOI: https://doi.org/10.2138/am-2022-8453. http://www.minsocam.org/

Figure 1

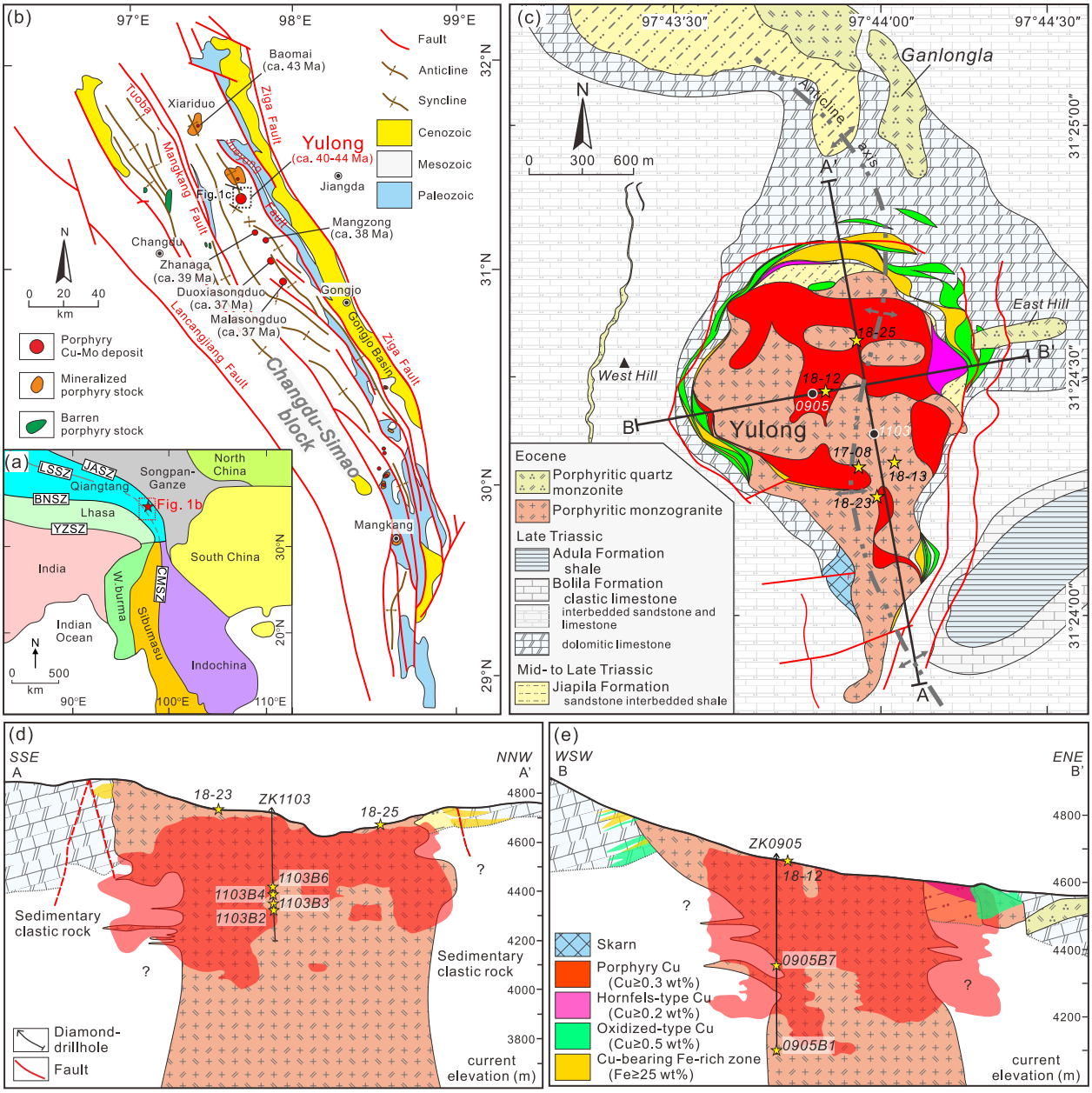

This is the peer-reviewed, final accepted version for American Mineralogist, published by the Mineralogical Society of America.
The published version is subject to change. Cite as Authors (Year) Title. American Mineralogist, in press.
DOI: https://doi.org/10.2138/am-2022-8453. http://www.minsocam.org/

Figure 2

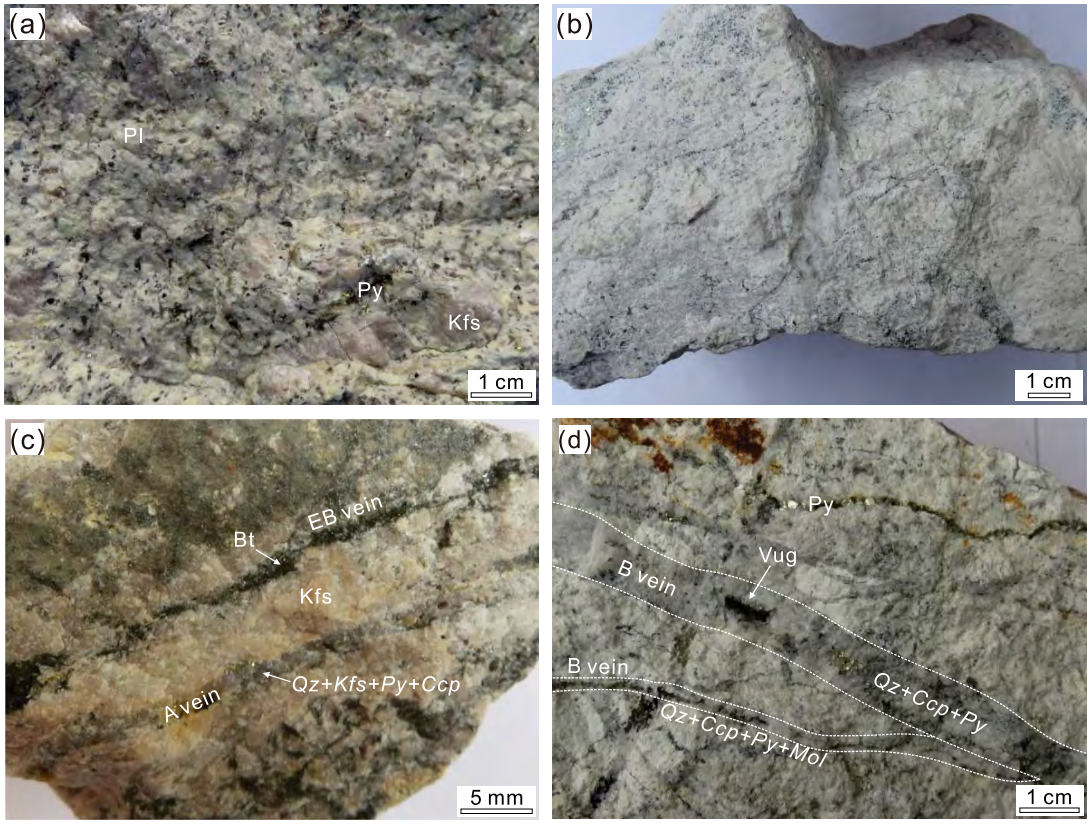

This is the peer-reviewed, final accepted version for American Mineralogist, published by the Mineralogical Society of America.
The published version is subject to change. Cite as Authors (Year) Title. American Mineralogist, in press.
DOI: https://doi.org/10.2138/am-2022-8453. http://www.minsocam.org/

Figure 3

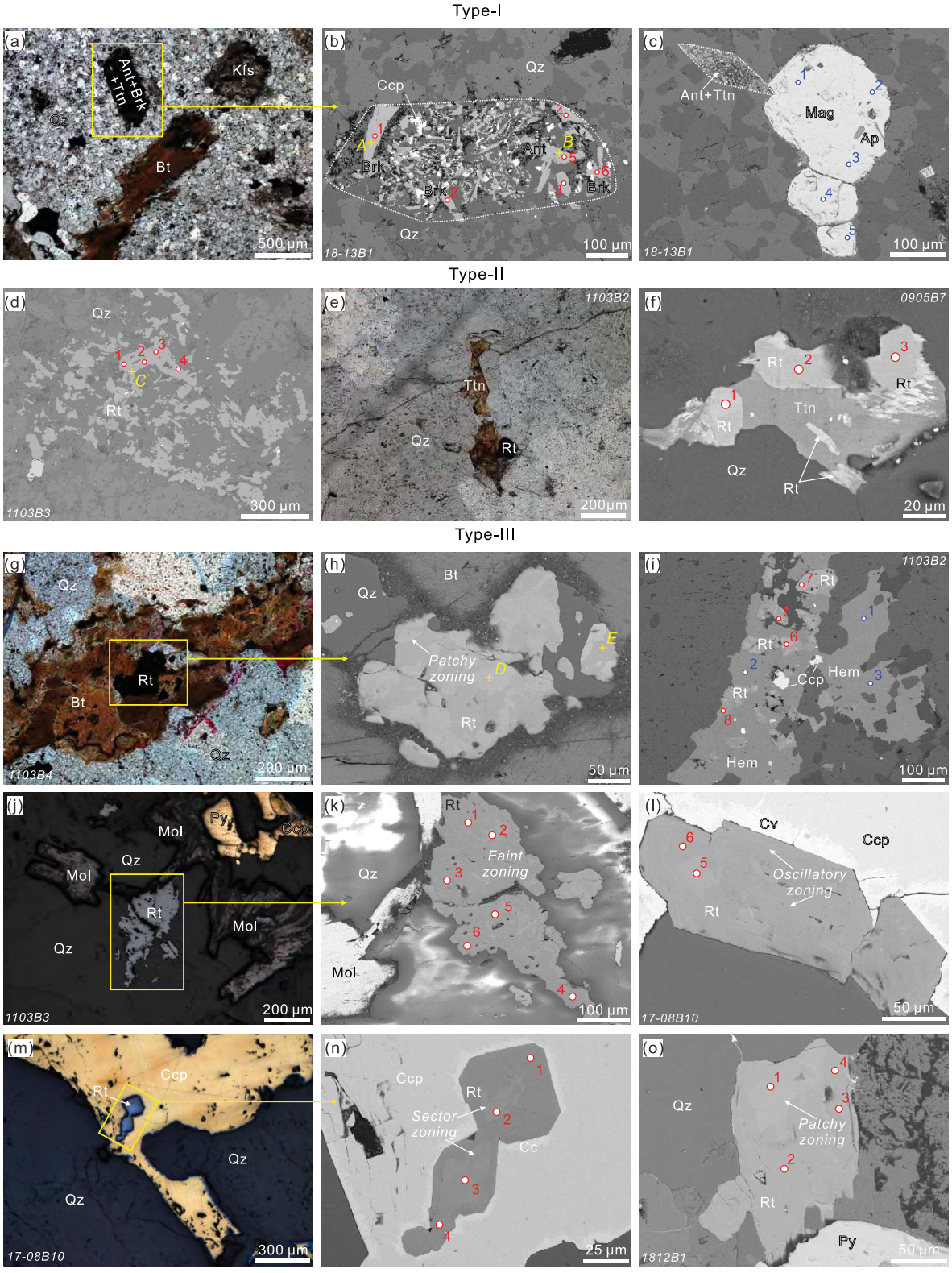

Figure 4

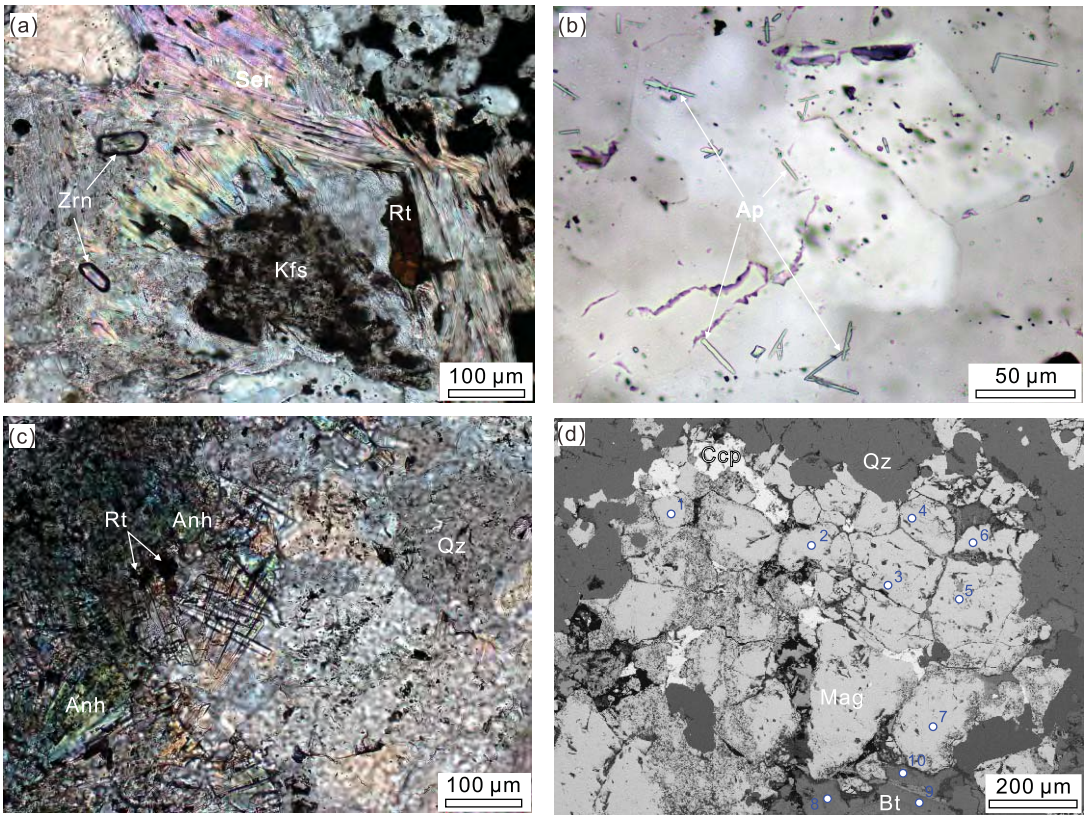

This is the peer-reviewed, final accepted version for American Mineralogist, published by the Mineralogical Society of America.
The published version is subject to change. Cite as Authors (Year) Title. American Mineralogist, in press.
DOI: https://doi.org/10.2138/am-2022-8453. http://www.minsocam.org/

Figure 5

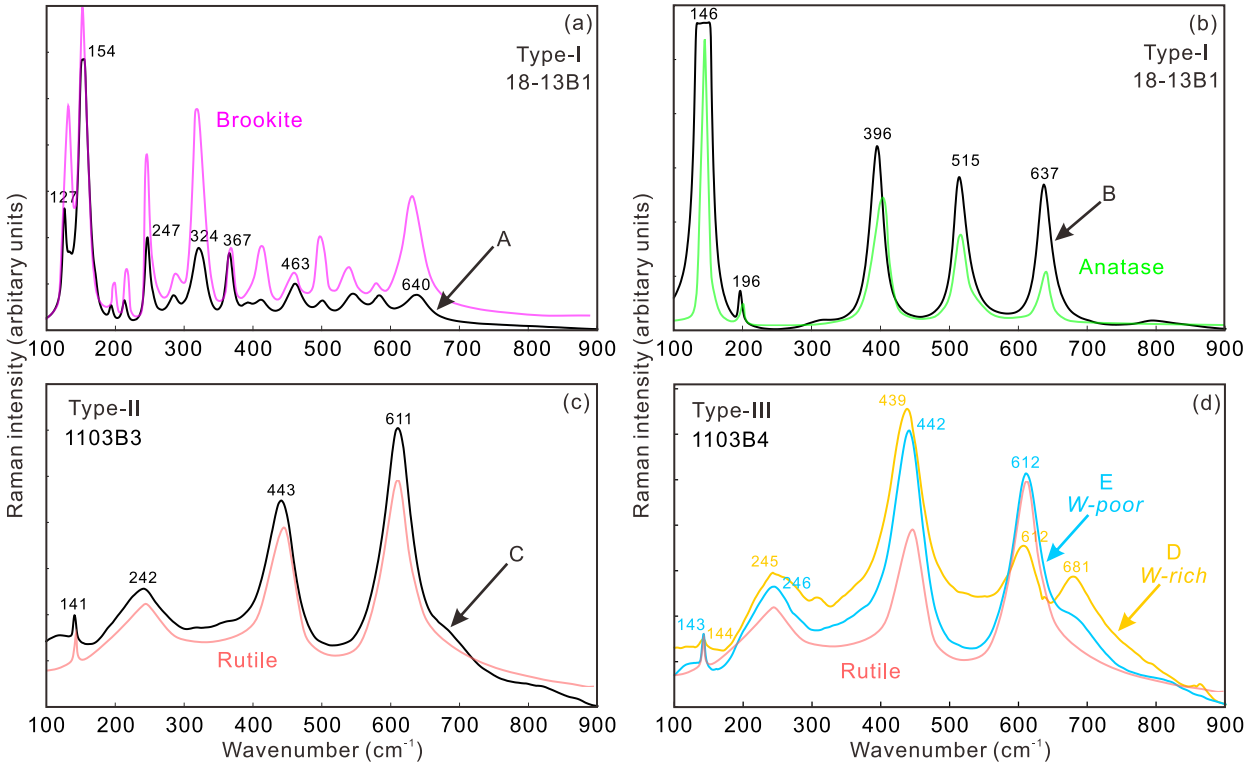

This is the peer-reviewed, final accepted version for American Mineralogist, published by the Mineralogical Society of America.
The published version is subject to change. Cite as Authors (Year) Title. American Mineralogist, in press.
DOI: https://doi.org/10.2138/am-2022-8453. http://www.minsocam.org/

Figure 6

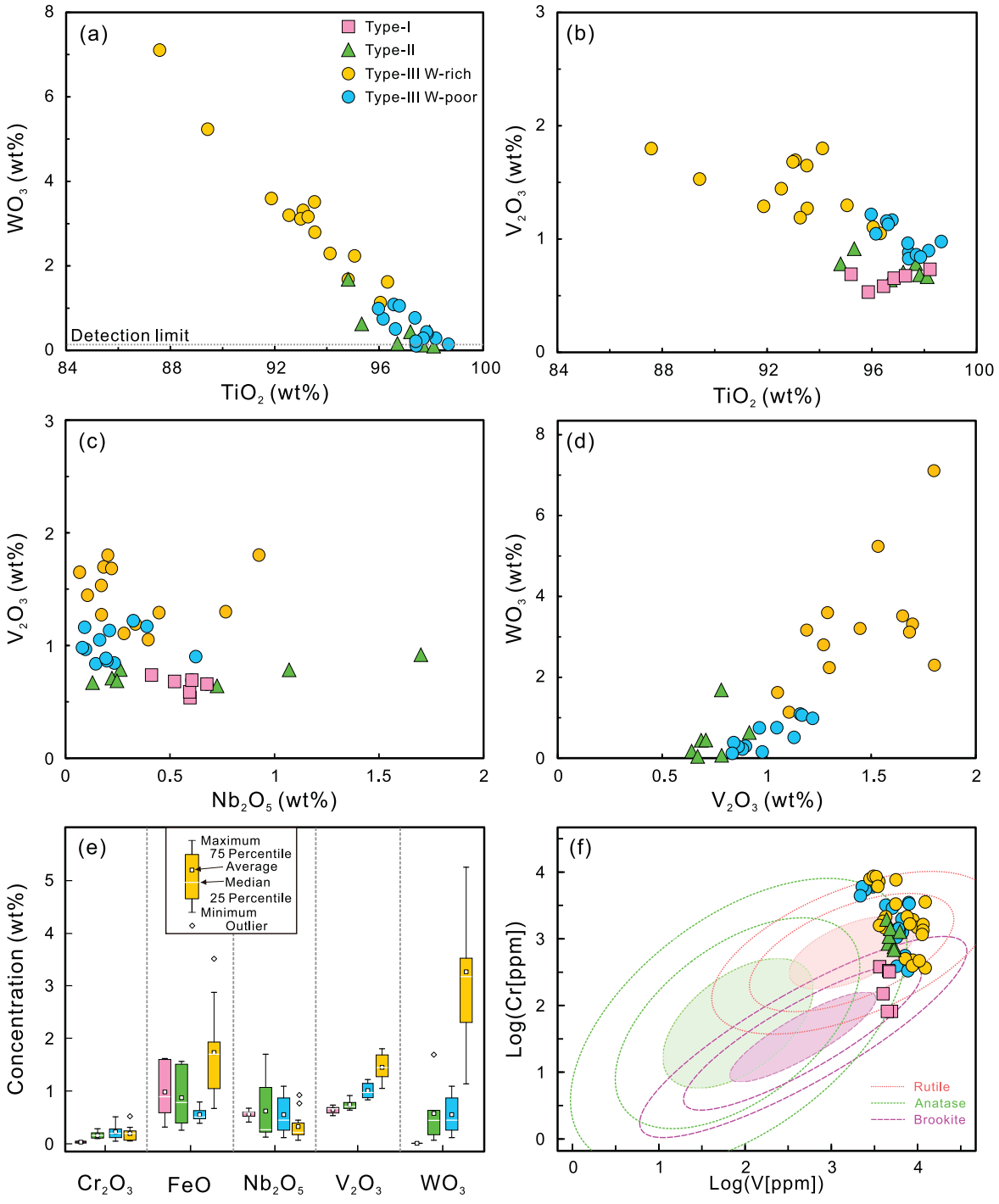

This is the peer-reviewed, final accepted version for American Mineralogist, published by the Mineralogical Society of America.
The published version is subject to change. Cite as Authors (Year) Title. American Mineralogist, in press.
DOI: https://doi.org/10.2138/am-2022-8453. http://www.minsocam.org/

Figure 7

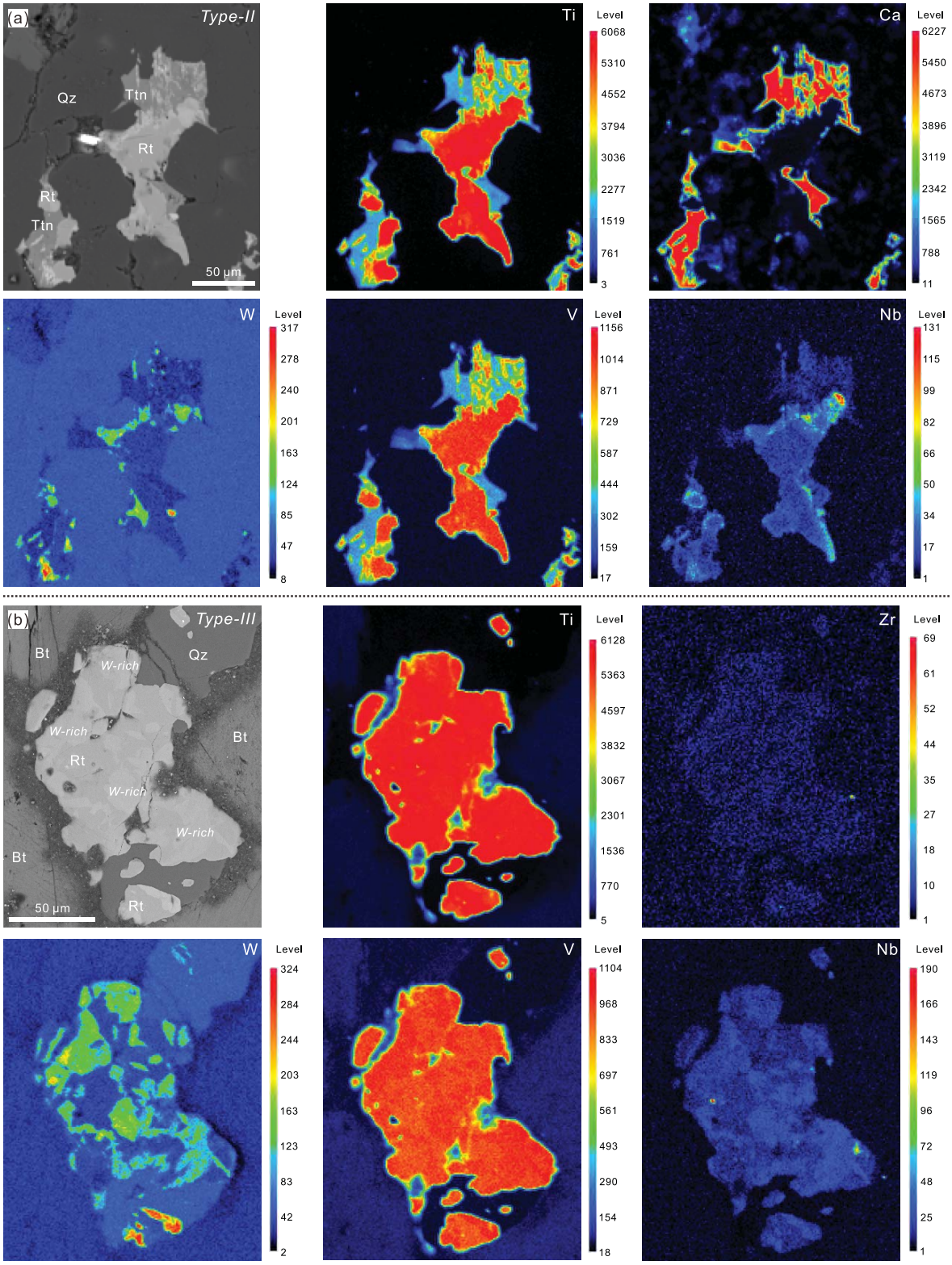

This is the peer-reviewed, final accepted version for American Mineralogist, published by the Mineralogical Society of America.
The published version is subject to change. Cite as Authors (Year) Title. American Mineralogist, in press.
DOI: https://doi.org/10.2138/am-2022-8453. http://www.minsocam.org/

Figure 8

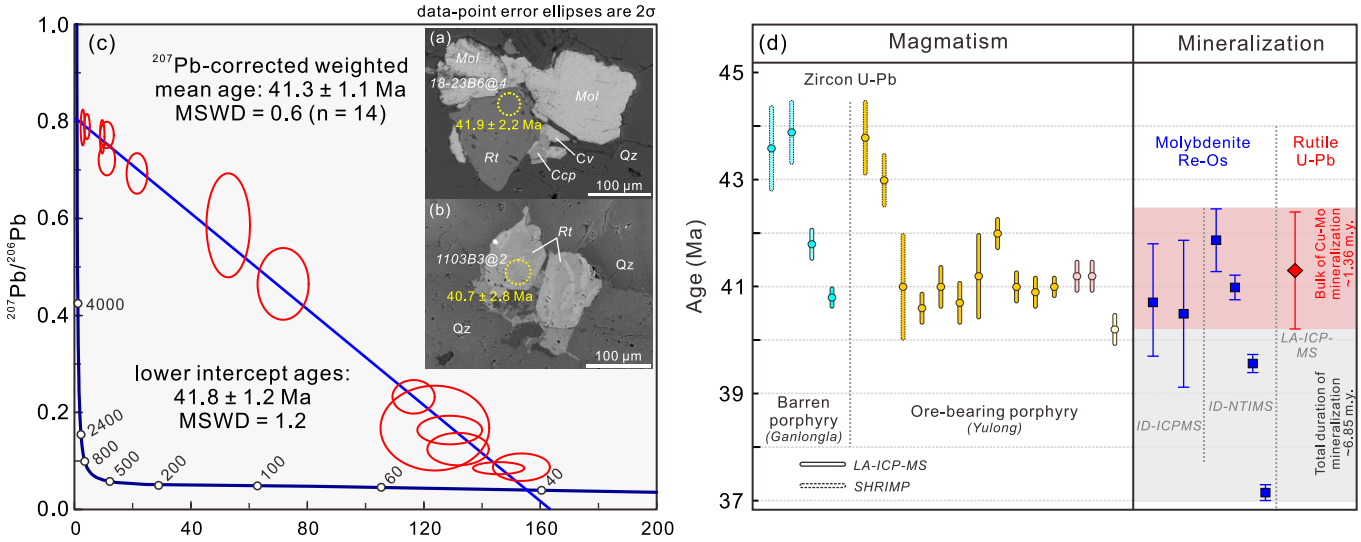

This is the peer-reviewed, final accepted version for American Mineralogist, published by the Mineralogical Society of America.
The published version is subject to change. Cite as Authors (Year) Title. American Mineralogist, in press.
DOI: https://doi.org/10.2138/am-2022-8453. http://www.minsocam.org/

Figure 9

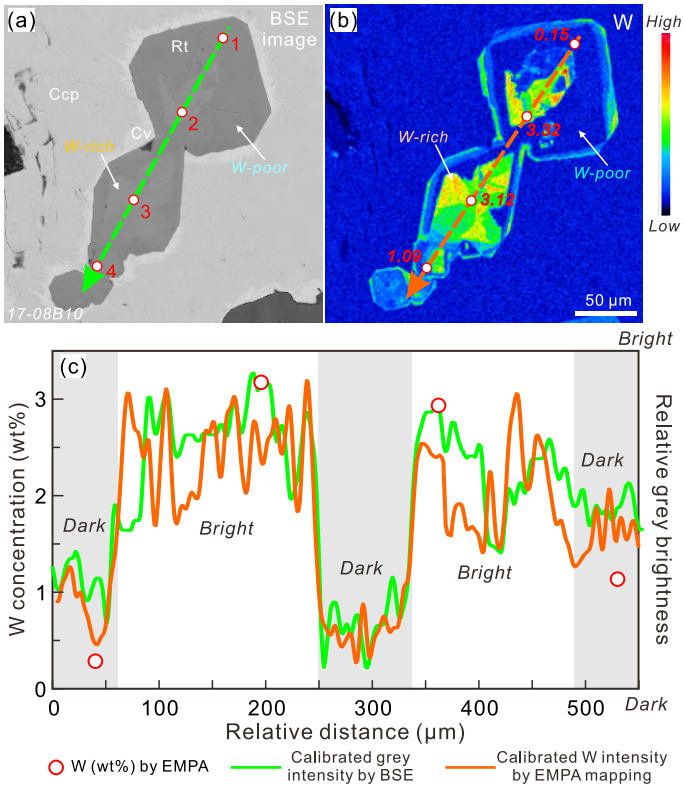

This is the peer-reviewed, final accepted version for American Mineralogist, published by the Mineralogical Society of America.
The published version is subject to change. Cite as Authors (Year) Title. American Mineralogist, in press.
DOI: https://doi.org/10.2138/am-2022-8453. http://www.minsocam.org/

Figure 10

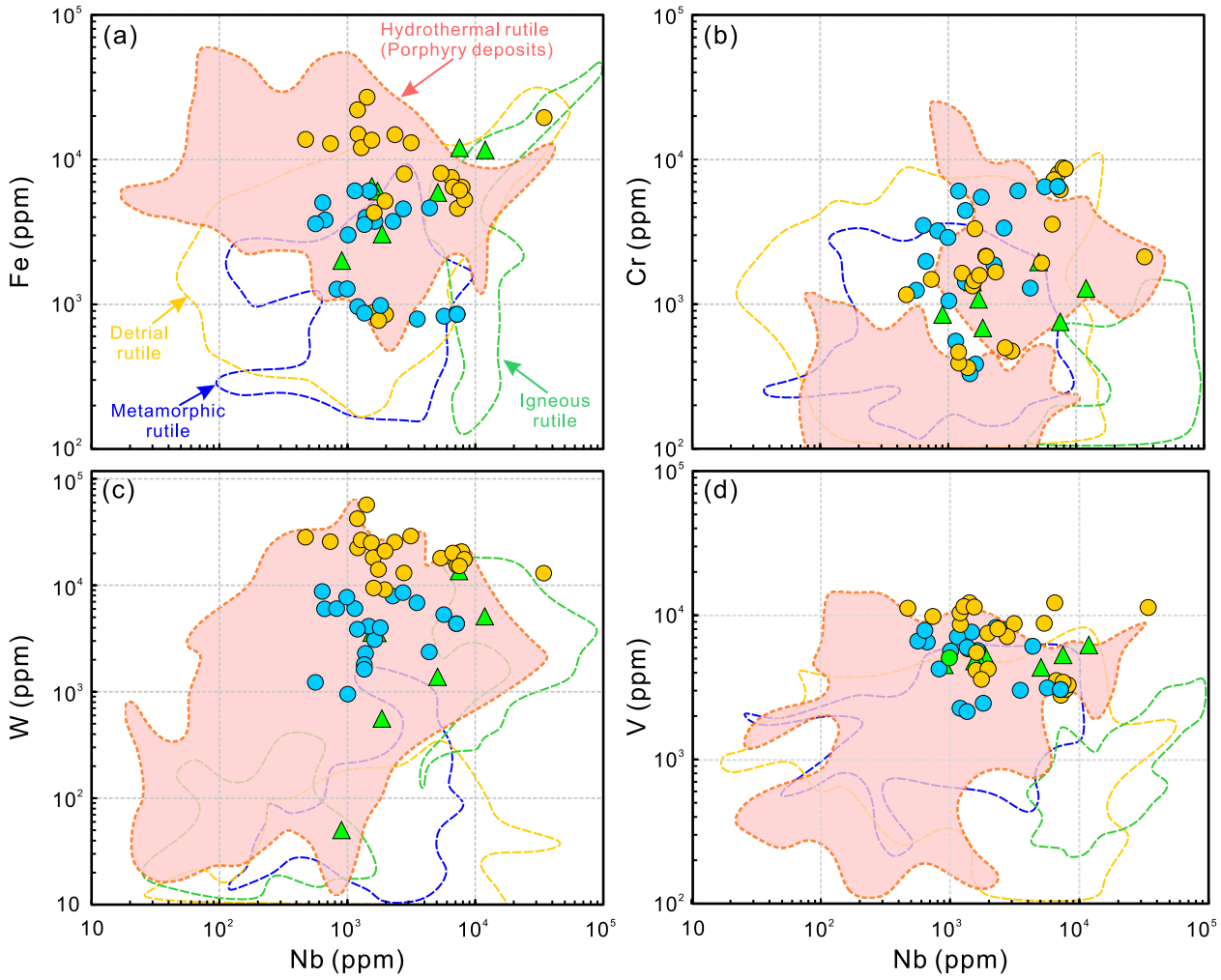

This is the peer-reviewed, final accepted version for American Mineralogist, published by the Mineralogical Society of America.
The published version is subject to change. Cite as Authors (Year) Title. American Mineralogist, in press.
DOI: https://doi.org/10.2138/am-2022-8453. http://www.minsocam.org/

Figure 11

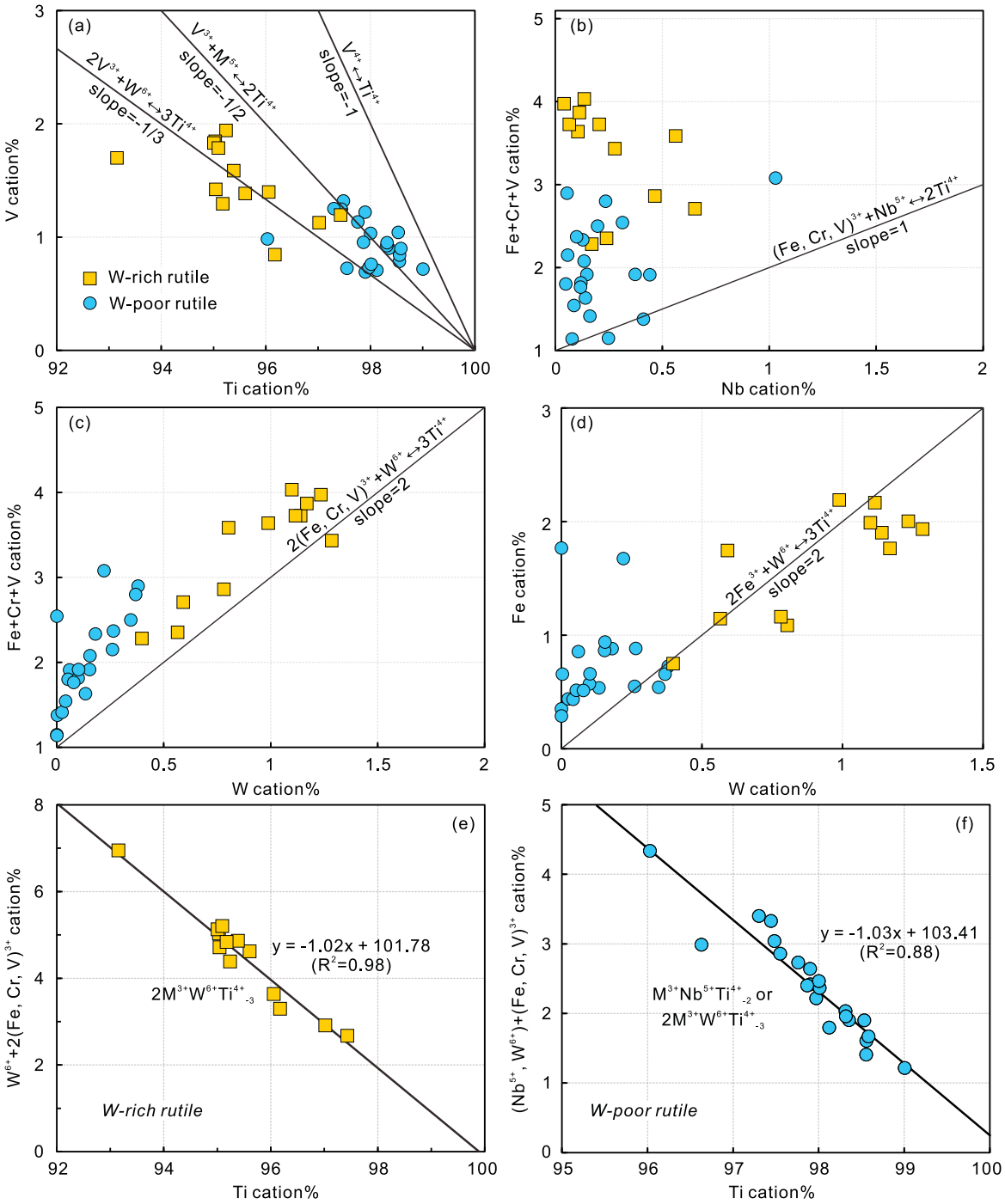

This is the peer-reviewed, final accepted version for American Mineralogist, published by the Mineralogical Society of America.
The published version is subject to change. Cite as Authors (Year) Title. American Mineralogist, in press.
DOI: https://doi.org/10.2138/am-2022-8453. http://www.minsocam.org/

Figure 12

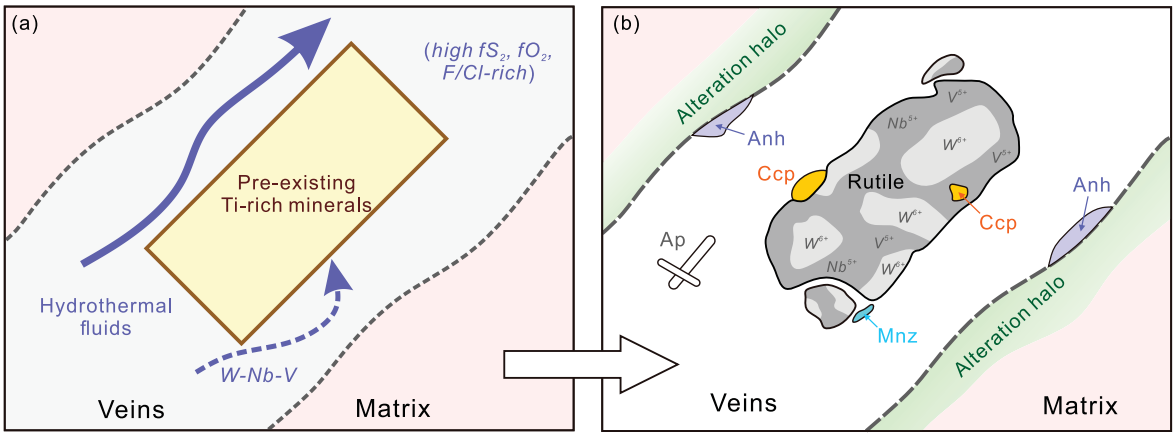

This is the peer-reviewed, final accepted version for American Mineralogist, published by the Mineralogical Society of America.
The published version is subject to change. Cite as Authors (Year) Title. American Mineralogist, in press.
DOI: https://doi.org/10.2138/am-2022-8453. http://www.minsocam.org/

Table 1. TiO_2 polymorphs textural features and assemblages in the Yulong Cu-Mo porphyry deposit

Types	Host rocks	Occurrence	Morphology	BSE texture
Type-I anatase and brookite	Fine-grained matrix of altered porphyritic monzogranite	Accessory hydrothermal altered mineral; pseudomorphic shape of titanite crystals contact with monazite, chalcopyrite, magnetite, and quartz	Subhedral, and fine grains Size: 20–200 μm	Homogeneous
Type-II rutile	Hydrothermal veins or alteration envelope of altered porphyritic monzogranite	Occurs alone or in clusters in veins or alteration envelope; completely replacing titanite or coexisting with residual titanite	Anhedral, elongated and prismatic grains Size: 50–300 μm	Faint zoning
Type-III rutile	Hydrothermal veins of altered porphyritic monzogranite	Hosted in biotite or hematite; intergrown with or included in pyrite, chalcopyrite and molybdenite	Anhedral, and irregular grains Size: 50–300 μm	Well-developed zoning patterns including oscillatory, patchy and sector zoning